Tectonics®

RESEARCH ARTICLE
10.1029/2022TC007630

Thermo-Kinematic Constraints on Restoration of the Eastern Sichuan Fold-And-Thrust Belt, South China

Qianqian Feng[1,2], Nansheng Qiu[1,2], Hang Wu[1,2], and Hemin Koyi[3,4]

[1]National Key Laboratory of Petroleum Resources and Engineering, China University of Petroleum, Beijing, China, [2]College of Geosciences, China University of Petroleum, Beijing, China, [3]Hans Ramberg Tectonic Laboratory, Department of Earth Sciences, Uppsala University, Uppsala, Sweden, [4]Now at Department of Earth Sciences, Khalifa University, Abu Dhabi, UAE

Key Points:

- New thermo-kinematic method combining analog modeling, discrete element method, balanced reconstruction, and thermochronology data
- Eastern Sichuan fold-and-thrust belt (ESFTB) experienced northwestward thrusting and periodic exhumation and its evolution can be subdivided into five stages
- Exhumation rate changes are responses of ESFTB to subduction retreat of the Paleo-Pacific Plate and eastward growth of the Tibetan Plateau

Supporting Information:

Supporting Information may be found in the online version of this article.

Correspondence to:

N. Qiu,
qiunsh@cup.edu.cn

Citation:

Feng, Q., Qiu, N., Wu, H., & Koyi, H. (2023). Thermo-kinematic constraints on restoration of the eastern Sichuan fold-and-thrust belt, South China. *Tectonics*, *42*, e2022TC007630. https://doi.org/10.1029/2022TC007630

Received 13 OCT 2022
Accepted 30 AUG 2023

Author Contributions:

Conceptualization: Qianqian Feng
Data curation: Qianqian Feng
Funding acquisition: Nansheng Qiu
Investigation: Qianqian Feng, Hang Wu
Methodology: Qianqian Feng, Hang Wu
Software: Hemin Koyi
Supervision: Nansheng Qiu, Hemin Koyi
Validation: Qianqian Feng
Visualization: Qianqian Feng, Hang Wu
Writing – original draft: Qianqian Feng, Hang Wu
Writing – review & editing: Nansheng Qiu, Hemin Koyi

Abstract Kinematic restoration of the eastern Sichuan fold-and-thrust belt (ESFTB) in South China is calibrated with a new thermo-kinematic model combining analog models, discrete element method, and thermochronology data. Thermo-kinematic analysis provides constraints on the onset, rate, and lateral variation of deformation and exhumation. Results show that the ESFTB experienced a northwestward thrusting and periodic exhumation. Its evolution was characterized by five major stages based on the deformation characteristics; (a) Shortening above a basal decollement and formation of large imbricates separated by narrow synclines during 170–130 Ma; (b) Transition stage during 130–100 Ma; (c) Stepping up of deformation to shallow decollement levels and shaping of the thick-skinned domain during 100–70 Ma; (d) Shaping of the thin-skinned domain during 70–20 Ma; and (e) Continuous exhumation and structural modification from 20 Ma to present. The changes in the exhumation rate have been tectonic responses to the subduction retreat of the Paleo-Pacific Plate and the eastward growth of the Tibetan Plateau. The westward subduction of the Paleo-Pacific Plate resulted in northwestward shortening across South China, progressive deformation of the ESFTB, and rapid exhumation from the Late Jurassic to the Late Cretaceous. The crustal extension associated with the rollback of the Paleo-Pacific slab accounted for the Mesozoic exhumation rate decrease until the Miocene. The accelerated cooling of the thin-skinned domain of the ESFTB since the Miocene was a response to the eastward growth of the Tibetan Plateau, while the continuous slow exhumation in the thick-skinned domain was related to the continuous crustal extension in South China.

1. Introduction

The eastern Sichuan fold-and-thrust belt (ESFTB) is located between the Sichuan Basin and the Jiangnan-Xuefengshan orogen in South China, and it is a large-scale intracontinental Jura-type fold-and-thrust belt with multiple décollements in the Yangtze Block (Chu, Faure, 2012; Chu, Lin, et al., 2012; Gu et al., 2021; C. X. Li et al., 2021; Shu et al., 2008; Y. J. Wang et al., 2013; Yan et al., 2003). The northeast-trending Qiyueshan fault (QYF) subdivides the ESFTB into three structural domains. The NW thin-skinned domain is characterized by narrow anticlines and broad synclines, while the SE thick-skinned domain is characterized by broad anticlines and narrow synclines and the middle transition domain is a large thrust nappe (Figure 1). Numerous studies have been conducted to reconstruct the tectonic evolution of the ESFTB through field investigations (Yan et al., 2009), seismic interpretation (Gu et al., 2015; C. X. Li et al., 2021; X. S. Zhu et al., 2020), analog models (W. G. He et al., 2018; Wu et al., 2020; Xie et al., 2013; Zhou and Zhou, 2022), numerical modeling (B. L. Zhang et al., 2009; X. Q. Zhang et al., 2013, 2015), balanced restoration (Gu et al., 2021; W. S. Hu et al., 2011; C. X. Li et al., 2021; Mei et al., 2010), and thermochronological analysis (X. M. Li & Shan, 2011; C. X. Li et al., 2021; Mei et al., 2010; Richardson et al., 2008; C. B. Shen et al., 2009; H. C. Shi et al., 2016). Different genetic models have been proposed to explain the structural features of the belt, including a box fold model (S. Z. Liu, 1995), a structural inversion model (Z. Q. Li et al., 2002), a fault-bend fold model (C. M. Feng et al., 2008; Yan et al., 2003; X. Q. Zhang et al., 2015), and a fault-propagation and buckle fold model (Ding et al., 2007). There is a general agreement that formation of the ESFTB involved multiple décollements during the Middle Mesozoic (Late Jurassic-Early Cretaceous). However, the deformation mechanisms related to the shortening involving multiple décollements and the conversion from the thick-skinned domain in the SE to the thin-skinned domain in the NW remain unclear.

Different exhumation histories have been proposed for ESFTB. Due to the limited kinematic constraints during modeling of the thermal history, the thermal paths constrained by the thermochronology data (Figure 2)

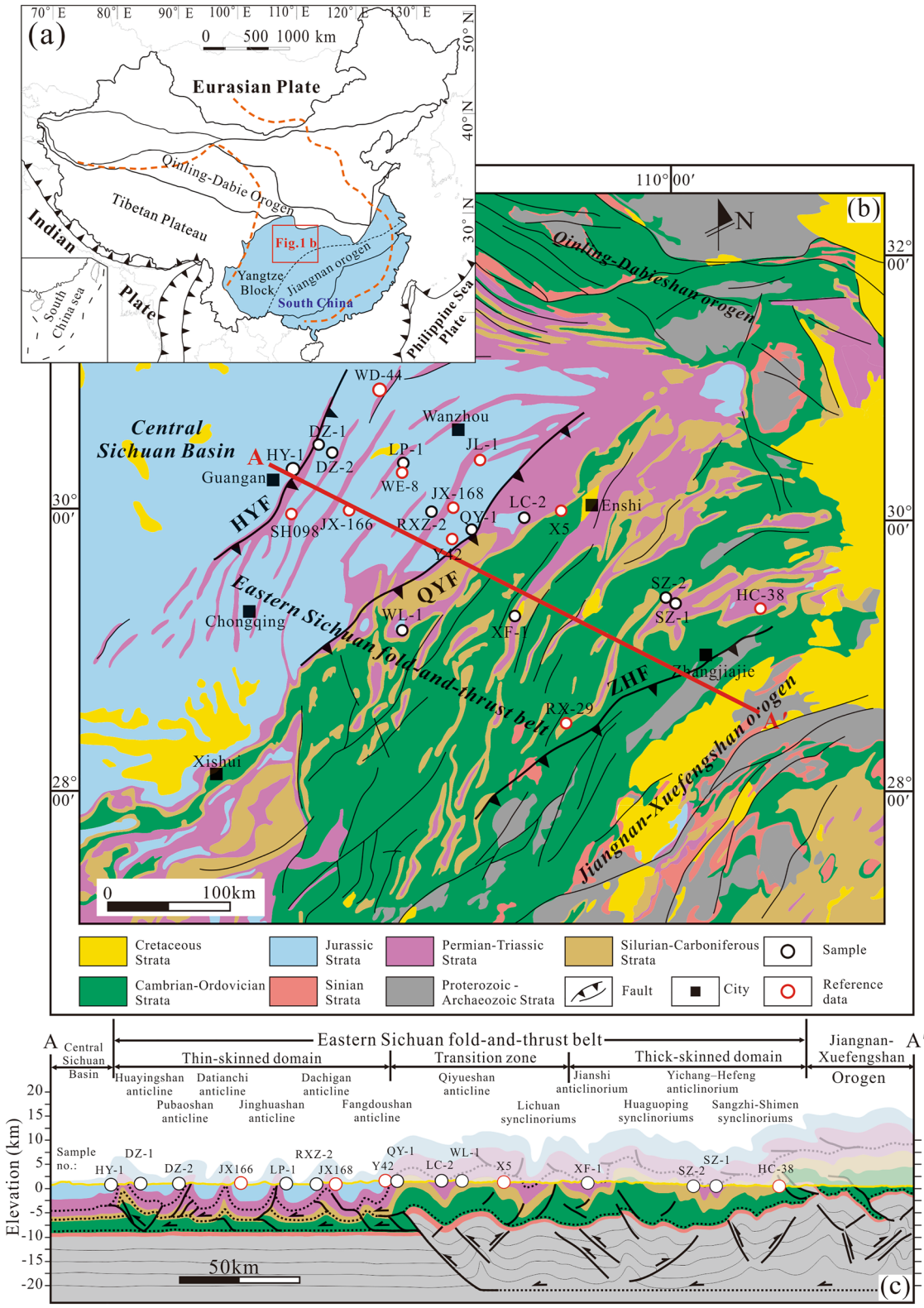

Figure 1.

suggest different scenarios for the Mesozoic-Cenozoic exhumation, including three stages of exhumation (rapid-slow-rapid) (Deng et al., 2013; X. M. Li & Shan, 2011; C. X. Li et al., 2021; Mei et al., 2010; Qiu et al., 2020; C. B. Shen et al., 2009; H. C. Shi et al., 2016), two stages of exhumation (slow-rapid) (S. J. Li et al., 2011; Richardson et al., 2008), and one stage exhumation (Tian et al., 2011; P. Wang et al., 2012). The thermal histories obtained from samples from different parts of the Qiyueshan area (a thrust sheet in the ESFTB) also indicate different onset times for the exhumation. Thermochronology analyses have shown that the onset of cooling ranged from 110 to 80 Ma (X. M. Li & Shan, 2011; Mei et al., 2010; Qiu et al., 2020; C. B. Shen et al., 2009; H. C. Shi et al., 2016). Located in the transitional zone between the Tethys-Himalayan and the Circum Pacific tectonic domain, the evolution of the ESFTB was controlled by prolonged subduction of the Paleo-Pacific Plate. Numerous studies on the thermochronological, structural, petrological, geochemical, and stratigraphic aspects have improved our understanding of the tectonic responses of South China to the subduction and rollback of the Paleo-Pacific Plate (Chu et al., 2019; Dong et al., 2020; Ji et al., 2018; J. H. Li et al., 2014, 2018, 2020; Z. Li et al., 2014; S. Z. Li et al., 2019; Suo et al., 2020; Sun et al., 2022). The eastward growth of the Tibetan Plateau due to the north-south India-Eurasia collision since the Early Cenozoic has been widely accepted (H. L. Li et al., 2020; Roger et al., 2010; X. M. Shen et al., 2019; Tian et al., 2013, 2016, 2018; Tong et al., 2019; E. Wang et al., 2003, 2012, 2014; Y. Wang et al., 2018; Yang et al., 2017). However, the tectonic response of the ESFTB to the subduction and rollback of the Paleo-Pacific Plate and the eastward growth of the Tibetan Plateau are poorly understood. The dynamic of multiphase cooling and exhumation in the ESFTB revealed by the thermochronological data remain ambiguous. The distinctive differential cooling of the Sichuan Basin in the Cenozoic is generally interpreted as a response to the far-field effects of the eastward growth of the Tibetan Plateau (Deng et al., 2013; X. M. Shen et al., 2019; H. C. Shi et al., 2016; Tian et al., 2012a, 2012b, 2013, 2018). However, the onset of the accelerated cooling in the Cenozoic is not well understood, and several hypotheses have been proposed. For example, Richardson et al. (2008) suggested an episode of accelerated cooling after 40 Ma in the thin-skinned domain. On the other hand, based on apatite fission track (AFT) data, Deng et al. (2013) suggested that the final accelerated cooling occurred at approximately 20–10 Ma along the Huayingshan, which is a thrust nappe in the thin-skinned domain. Furthermore, based on low-temperature thermochronology (AFT and apatite (U-Th)/He, AHe) data, Tian et al. (2018) determined that distinctive accelerated cooling occurred at ~35–28 Ma in the eastern Sichuan Basin. Thermal histories constrained by H. C. Shi et al. (2016) indicate that the onset of the final-stage cooling to surface temperatures occurred at 20–15 Ma. In summary, due to a lack of AHe data, whether or not the thick-skinned domain experienced differential cooling during the Cenozoic is still unclear. Thus, conducting an AHe study of the thick-skinned domain is a key element in determining the Cenozoic exhumation history of the ESFTB.

To address these questions, we have constructed a NW-SE striking balanced geological cross-section and collected new apatite fission-track, apatite (U-Th)/He, and zircon (U-Th)/He (ZHe) data from the major thrust sheets in the area. We also developed a forward two-dimensional (2D) analog model with 4 décollement layers and compared it with the results of a corresponding numerical model using the discrete element method (DEM). Based on analog models, we obtained several kinematic constraints for the thermal modeling and determined the timing and magnitude of the shortening of the thrust sheets. The structural and thermochronology data were combined in a thermo-kinematic model to calibrate the sequential restoration of the balanced geological cross-section, and then, we reconstructed the tectonic evolution of the ESFTB using the 2Dmove software. By comparing the differences in exhumation in the major thrust sheets, we further investigated the tectonic response to the subduction and rollback of the Paleo-Pacific Plate and the eastward growth of the Tibetan Plateau during the Mesozoic-Cenozoic. The thermo-kinematic modeling conducted in this study provides comprehensive constraints on the timing and magnitude of the shortening, as well as the structural evolution and deformation of the ESFTB.

Figure 1. (a) Simplified tectonic map of part of southeast Asia showing the location of the study area (modified after Jiang et al., 2019); (b) Geological map of the eastern Sichuan fold-and-thrust belt, modified after Z. Q. Hu et al. (2009), Xie et al. (2013), and Yan et al. (2003). The red and black circles indicate location of the test and reference samples, respectively. HYF: Huayingshan fault, QYF: Qiyueshan fault, ZHF: Zhangjiajie-Huayuan fault; (c) Geological cross-section A-A', interpreted based on the seismic profiles from Dong et al. (2015), C. X. Li et al. (2015, 2021). Trace of the section and the positions of the low-temperature thermochronology samples are shown in (b). The yellow and dotted bold black lines indicate the surface and the décollement layer, respectively. The eroded part is filled with light color according to the published data from X. Q. Zhang et al. (2015). The sample positions (empty circles and abbreviations above them) were projected onto the section along strike.

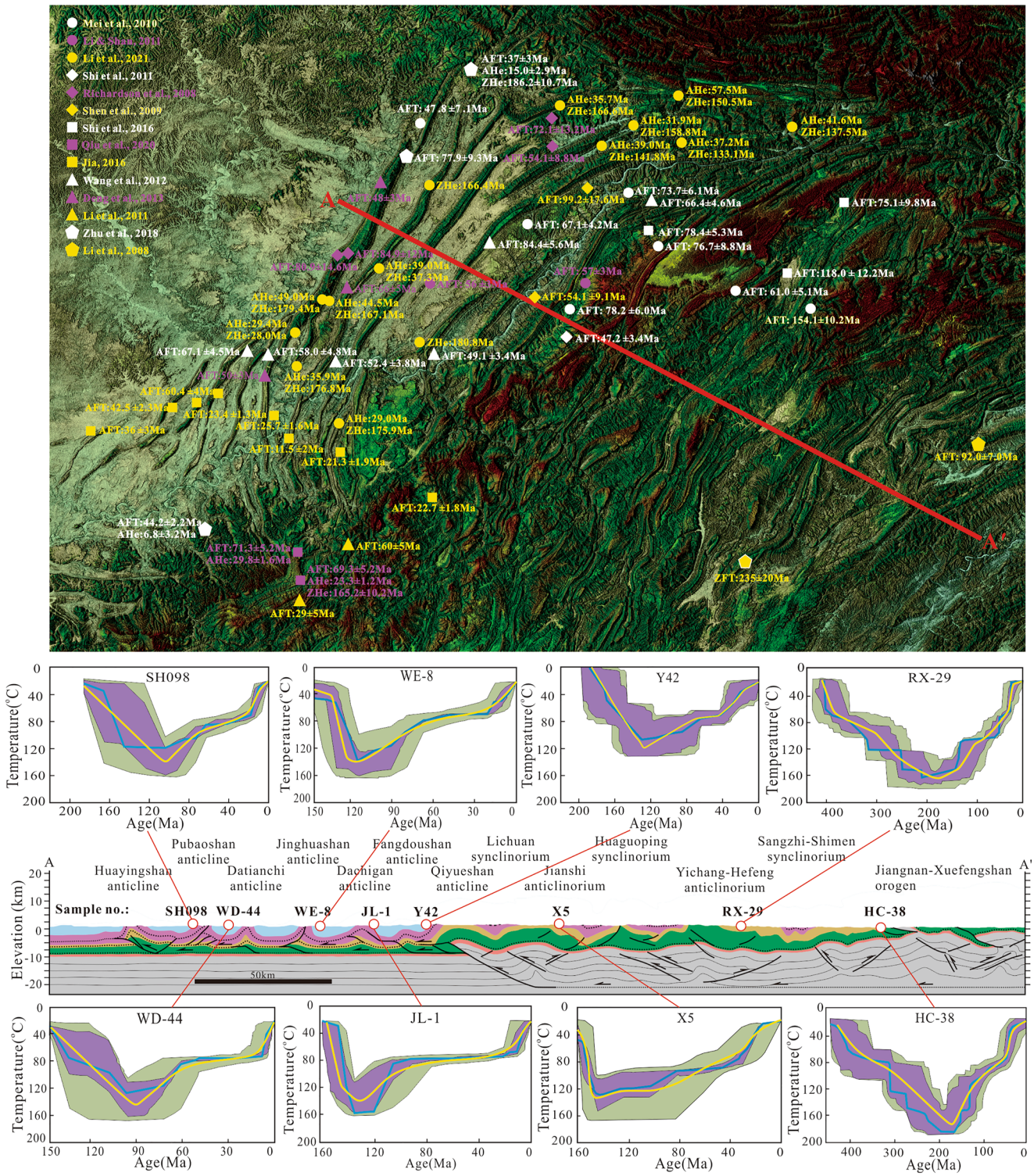

Figure 2. (a) Regional distribution of previous thermochronological ages (Ma ± 1σ errors) in the Eastern Sichuan fold-and-thrust belt (ESFTB). White point-Mei et al. (2010), pink point-X. M. Li and Shan (2011), yellow point-C. X. Li et al. (2021), white diamond-H. C. Shi et al. (2011), pink diamond-Richardson et al. (2008), yellow diamond-C. B. Shen et al. (2009), white square-H. C. Shi et al. (2016), pink square-Qiu et al. (2020), yellow square-Jia (2016), white triangle-P. Wang et al. (2012), pink triangle-Deng et al. (2013), yellow triangle-S. J. Li et al. (2011), white pentagon-C. Q. Zhu et al. (2017), yellow pentagon-S. J. Li et al. (2011). (b) Statistics of thermal histories in the ESFTB. Structural map of the study area (Figure 1) showing the location of section A-A' and of samples taken for thermochronologic analysis. Thermal history plots are shown for the different locations shown in the cross section. HC-38 and RX-29 based on S. J. Li et al. (2008); WE-8, WD-44, JL-1, and X5 based on Mei et al. (2010); Y42 based on H. C. Shi et al. (2016). SH098 based on Deng et al. (2013).

2. Geologic Setting

2.1. Structural Framework and Stratigraphy

The ESFTB is located in the Yangtze Block and is bounded by the Qinling-Dabieshan orogen to the north, the Jiangnan-Xuefengshan orogen to the east, and the Tibetan Plateau to the west (Figure 1a). The structural framework of the ESFTB has been described by many authors as multilayer décollement propagation, thin-skinned tectonics, and fault-related folding (C. X. Li et al., 2021; Yan et al., 2009). This Mesozoic fold-and-thrust belt has a total width of 400 km and is composed of a number of NE-NNE-striking subparallel folds, including the Huayingshan, Pubaoshan, Datianchi, Jinghuashan, Dachigan, Fangdoushan, and Qiyueshan anticlines; the Lichuan, Huaguoping, and Sangzhi-Shimen synclinoriums; and the Jianshi and Yichang-Hefeng anticlinoriums (Figures 1b and 1c). Geological cross section A-A' (interpreted from a seismic reflection profile and the surface geology) crosses the central part of the ESFTB and shows that the belt is affected by three major regional faults: the Huayingshan fault (HYF), the QYF, and the Zhangjiajie-Huayuan fault (ZHF) (Figure 1). These faults separate the ESFTB into three regions: a thin-skinned domain, a transition zone, and a thick-skinned domain (Figure 1c). The thin-skinned domain is composed of a series of high-amplitude, tight, and approximately upright anticlines (C. X. Li et al., 2021). The crests of the anticlines reach elevations of 500–800 m (C. X. Li et al., 2015), and each individual fold axis extends for 50–200 km (Yan et al., 2009). The transition zone consists of the Qiyueshan anticline and Lichuan synclinorium. In contrast, the thick-skinned domain contains several box anticlines separated by tight, chevron synclines (Figure 1c).

The Precambrian basement is covered by 5,000–10,000 m of sediments in the ESFTB (S. G. Liu et al., 2021). These sediments include a Paleozoic to Middle Triassic marine sequence and an Upper Triassic to Eocene terrestrial sequence (Figure 3). In the thin-skinned domain, the outcropping lithologies are mainly composed of Jurassic and Cretaceous sandstones and mudstones, while the Triassic strata are exposed in the eroded anticlinal cores. In the thick-skinned domain, there is a significant change in the outcropping strata. The anticlines have Cambrian to Ordovician strata in their cores and the synclines have Silurian to Permian strata in their troughs (Yan et al., 2009).

2.2. Pre-Existing Faults and Multilayer Décollements

HYF and QYF are two major pre-existing faults in the ESFTB. As the demarcation fault (boundary fault) between the central Sichuan Basin and the ESFTB, the HYF has a total length of 400 km and has been active since the Caledonian (Mei et al., 2010). Interpreted seismic data shows that the QYF is a reverse basement fault with a dip angle of 30°–40° (Dong et al., 2015; J. P. Hu et al., 2005; X. S. Zhu et al., 2020). X. Q. Zhang et al. (2015) speculated that the QYF was reactivated frequently and the shallow segment of the fault has rotated clockwise and became gentler since the Late Jurassic.

Four major décollement levels are recognized regionally in the ESFTB: (a) basal décollement horizon, (b) Middle-Lower Cambrian décollement, (c) Silurian décollement, and (d) Middle-Lower Triassic décollement (Figure 3). It is suggested that the basal décollement horizon is located in the Archean strata of the middle crust (Dong et al., 2015). The overall geometry of the middle crust on the seismic-reflection profile indicates the existence of crustal-scale imbrications, with thrust sheets stacked above a major décollement originating at a depth of >21 km (Dong et al., 2015). Other 3 décollement levels are located at different depths (Figure 1). The Middle-Lower Cambrian décollement layer, which is approximately 500–1,000 m thick, is mainly composed of the shale of Qiongzhusi Formation and gypsum and halite of the Gaotai-Longwangmiao Formation. The Silurian décollement layer includes the shale of the Hanjiadian and Longmaxi formations and has an average thickness of 1,500 m. However, the sand content of the Silurian strata is significantly higher in the thick-skinned domain (S. G. Liu et al., 2011), and the Xiaoheba Formation sandstone was deposited in this region. Furthermore, field outcrops, exploration wells, and seismic profiles show that the Silurian strata are generally involved in the thrusting (C. X. Li et al., 2021). These observations indicate that the décollement efficiency of the Silurian in the thick-skinned domain is weak, which is consistent with the results of a finite element numerical simulation (Xie et al., 2013). The Middle-Lower Triassic décollement layer has an average thickness of approximately 1,050 m, and is composed of gypsum-bearing dolomite and oolitic limestone interbedded with marl and mudstone (Jialingjiang and Leikoupou formations) (C. X. Li et al., 2015).

2.3. Tectonic Evolution

Because of its location in the transition zone between the Tethys-Himalayan and the Circum Pacific tectonic domains, the Yangtze Block experienced multiple major tectonic episodes from the Paleozoic to the Cenozoic,

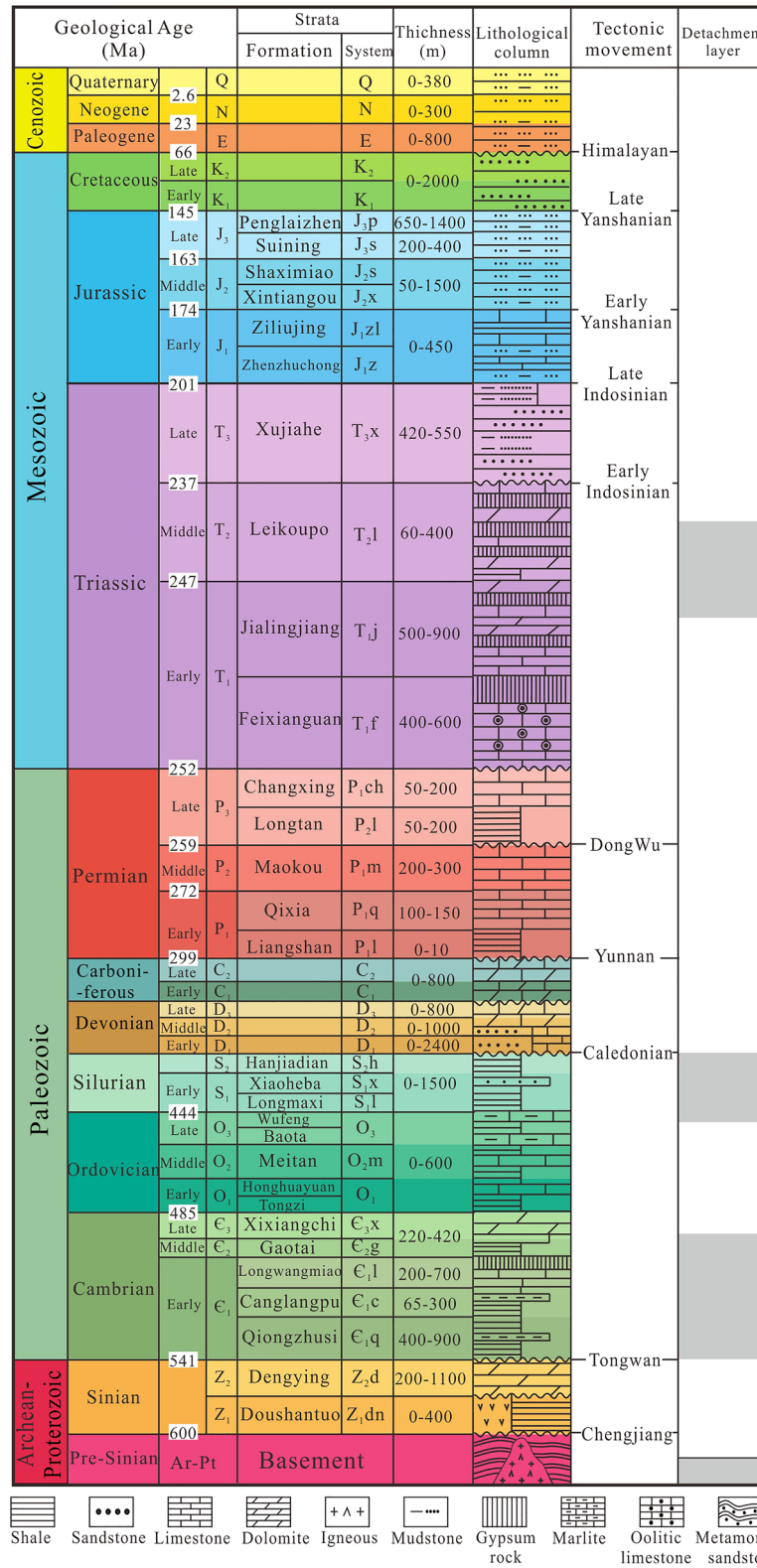

Figure 3. Stratigraphic column of the eastern Sichuan fold-and-thrust belt, modified after C. X. Li et al. (2015).

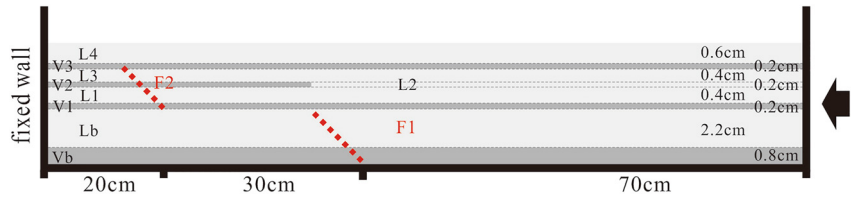

Figure 4. Schematic profile showing the initial model setup of the analog models. The dotted red lines (F1 and F2) represent pre-existing faults. Four viscous layers (dark gray layers), from bottom to top, namely Vb, V1, V2, and V3, respectively, represent four weak horizons. The light gray layers (Lb, L1, L2, L3, and L4) represent brittle layers.

including the Caledonian, Hercynian, Indosinian, Yanshanian, and Himalayan orogens (Figure 3). Deformation since the Early Cretaceous created the present structural features (Yan et al., 2003; Yong et al., 2018). Based on distribution of folds and faults, several studies suggested that the ESFTB was mainly controlled by SE-NW compression during the Yanshanian tectonic period (Early Cretaceous-Eocene) and approximately E-W compression during the Himalayan tectonic period (Eocene-present) (Deng et al., 2013; S. G. Liu et al., 2021; Tian et al., 2018; Tong et al., 2019; E. Wang et al., 2014). However, using low-temperature thermochronology data, several researchers suggested that the ESFTB has experienced three major tectonic phases since the Mesozoic: (a) northwestward thrusting caused by the northwestward subduction of the Paleo-Pacific Plate underneath the Eurasian Plate during the Late Jurassic-Late Cretaceous; (b) a slow denudation phase in response to the back-arc extension within South China due to the rollback of the Paleo-Pacific slab during the Late Cretaceous-Miocene; and (c) a rapid denudation phase caused by propagation of the far-field stress during the southeastward growth of the Tibetan Plateau from the Miocene to present (S. J. Li et al., 2008; Mei et al., 2010; Richardson et al., 2008; H. C. Shi et al., 2016; Tian et al., 2012a, 2012b, 2018; Wu et al., 2020).

3. Methods

In this study, balanced-section restoration of profile A-A' is calibrated with the thermo-kinematic model using combined results of analog models, DEM, and thermochronology data. By compiling surface structural geology and age data set of Late Mesozoic magmatic rocks in South China, a single distinctive tectonic switch at ~170 Ma was defined and it is generally believed that significant crustal shortening occurred during the period of 170–135 Ma, followed by crustal extension during the period of 135–80 Ma (Chu et al., 2019; J. H. Li et al., 2020; Y. Q. Zhang et al., 2021). It is generally believed that the Mesozoic crustal shortening and extension resulted in the establishment of the ESFTB (Chu et al., 2019; C. X. Li et al., 2021; Yan et al., 2003, 2009; Zhou and Zhou, 2022). Furthermore, based on the thermochronological analysis previous studies suggested that the ESFTB experienced progressive deformation during a three-phases of cooling (Figure 2b): (a) rapid cooling during ~170–70 Ma, (b) slow cooling during ~70–30[?] Ma, and (c) accelerated cooling from ~30[?] Ma to present (S. J. Li et al., 2008; Mei et al., 2010; Richardson et al., 2008; H. C. Shi et al., 2016; Tian et al., 2012a, 2012b, 2018; Wu et al., 2020). It is generally believed that the rapid cooling during ~170–70 Ma is associated with thrusting. According to the tectonic evolution, it can be determined that thrusting occurred in the area of profile A-A' during 170–70 Ma. Therefore, we set the time period ~170-70 Ma as constraints for the analog modeling, particle flow code (PFC2D) modeling and thermo-kinematic modeling.

3.1. Analog Models

In this study, one set of analog models was conducted to reconstruct deformation along profile A–A'. The analog models were conducted in a 120 cm × 20 cm plexiglas box filled with layers of loose glass micro-beads and silicone, which simulated the brittle and viscous rheologies, respectively (Figure 4). Glass micro-beads, which is a Coulomb material, is commonly used to simulated non-evaporitic sediments. Mechanically, they are weaker than dry quartz sand and have almost no cohesion (Bonnet et al., 2007; Konstantinovskaya et al., 2009; Massoli et al., 2006; Teixell & Koyi, 2003). We used glass micro-beads to simulate the frictional behavior of the brittle overburden. The silicone putty (produced by Beijing Dingye Chemical Ltd of China) which is a Newtonian fluid, simulated the ductile behavior of the weak décollements. The silicone polymer had a density of ~0.94 g/cm ^{3} and a viscosity (measured using a numerical Brookfield Type viscometer at room temperatures) of 1.0×10^4 Pa s. The sieved glass micro-beads had a bulk density of ~1.48 g/cm^3 and a grain size of 180–250 μm. The internal

Table 1
Scaling Parameters Between the Sandbox Analog Models and Nature

Parameter	Model	Nature	Model/nature ratio (*)
ρ_b (g/cm^3)	1.48	2.6	$\rho_b^* = 0.57$
ρ_d (g/cm^3)	0.94	2.2	$\rho_d^* = 0.43$
μ	0.7	0.6–0.85	$\mu^* = 0.55$–1.17
c (Pa)	99	4×10^7	$c^* = 2.48 \times 10^{-6}$
g (m/s^2)	9.81	9.81	$g^* = 1$
η (Pa s)	1×10^4	5×10^{20}	$\eta^* = 2 \times 10^{-17}$
l (m)	0.01	5,000	$l^* = 2 \times 10^{-6}$
σ (Pa)	578.1	5.24×10^8	$\sigma^* = 1.1 \times 10^{-6}$
ε (/s)	8.3×10^{-4}	1.42×10^{-13}	$\varepsilon^* = \sigma^*/\eta^* = 5.5 \times 10^{10}$
v (cm/hr)	2.4	2.1×10^{-5}(0.18 cm/yr)	$v^* = l^* \times \varepsilon^* = 1.1 \times 10^5$

Note. ρ_b-density of the brittle overburden strata from the basement to the Jurassic; ρ_d-density of the ductile décollement; μ-internal friction coefficient of the brittle overburden; c-cohesion of the brittle overburden; g-gravity acceleration; η-viscosity of the ductile décollement; l-length; σ-stress ($\sigma = \rho_b g h_b$, $+\rho_b g h_{d1}$, h_b, and h_{d1}-thickness of the brittle and ductile overburden strata from the basement to the Jurassic, respectively.); t-time; ε-strain rate ($\varepsilon = v/h_{d2}$, h_{d2}-thickness of the basal viscous layer).

friction coefficient and internal friction angle of the micro-beads were 0.70° and 25°, respectively. A 0.8-cm thick basal viscous layer (V_b) was placed at the bottom of the plexiglas box to simulate the basal décollement. This was covered by a 4.2-cm thick layer of glass micro-beads (Lb-L4) interbedded with viscous layers (V1–V3) to simulate the basement to the Jurassic overburden strata. Viscous layers V1–V3 represented the Cambrian, Silurian, and Triassic décollement layers, respectively (Figure 4). We placed two pieces of smooth cardboard with a thickness of 0.2 mm in the box during the formation of the layers to simulate the pre-existing faults, that is, QYF (F1) and HYF (F2). Fault F1 was located between ductile layers Vb and V1, and fault F2 was located between ductile layers V1 and V3 (Figure 4). Interpreted seismic data shows that the HYF and QYF have dip angles of 30°–40°. Considering the pre-existing faults may change dip with time, we set a dip angle of 45°. Because the Silurian décollement (L2) did not have a significant impact on deformation in the thick-skinned domain, we only set the Silurian décollement layer (V2) in the foreland of F1, that is, in the thin-skinned domain (Figure 4). Erosion was not performed in the analog models.

The parameters used in the models and measured in nature are presented in Table 1. Restoration of the balanced geological cross-section (A-A') revealed that the ESFTB experienced a total shortening of ~140 km (~24% shortening) (W. G. He et al., 2018) and the shortening rate was 0.1–0.2 cm/yr during the Late Jurassic-Cretaceous (C. X. Li et al., 2015). In this study, assuming some uncertainty in the restoration, we set the maximum shortening ratio of cross-section A-A' to 30% (i.e., the initial length of this section was 600 km and shortened to 420 km). The model was scaled to nature with a length ratio (l*) of 2×10^{-6} (i.e., 1 cm in the model represented 5 km in nature). The density of the brittle overburden (ρ_b) and the density of the weak décollement (ρ_d) in nature are 2.60 and 2.20 g/cm^3, respectively (Cotton & Koyi, 2000). The internal friction coefficient (μ) and cohesion of the brittle overburden (c) in nature are 0.60–0.85 and ~4×10^7 Pa, respectively (Bonini, 2003, 2007; Costa and Vendeville, 2002; Zhou and Zhou, 2022). The viscosity of the weak décollement (η) in nature is assumed to be ~10^{20} Pa s (Bonini, 2007; Zhou and Zhou, 2022). The cohesion of the glass micro-beads (c) in the model was ~99 Pa (Yan et al., 2016). Accordingly, the model-to-nature ratios of the cohesion c^* and stress σ^* were 2.48×10^{-6} and 1.1×10^{-6}, respectively (Table 1), which are of the same order of magnitude, suggesting that the analog model fulfills the dynamic similarity criterion (Bonini et al., 2012; Cotton & Koyi, 2000). According to the model-to-nature ratios; strain rate ε^*, time t^*, and shortening velocity v^*, it is estimated that applying a shorting velocity of 2.4 cm/hr for 15 hr in the experiments, corresponds to 100 Ma of shortening in nature at a velocity of 0.18 cm/yr (Table 1).

3.2. Discrete Element Method

The DEM can be used to simulate the mechanical behavior of a system that consists of a collection of particles with different sizes. The two-dimensional PFC2D has been demonstrated to be a suitable tool for the simulation of a granular material (Cundall & Strack, 1979), and the Itasca Consulting Group developed the software package. The software allows for multiple interactions between rigid particles, such as contacts, bonds, overlapping, and breaking. The physical parameters of the interacting particle can be defined, including the density, contact stiffness, and friction. All of the contact forces, including the normal and shear forces, acting on a single particle are calculated together following Newton's law to determine the particle displacements. PFC2D has been widely used to simulate the mechanics and kinematics of geological structures, including gravitational volcanic deformation (Morgan, 2005), slope failure (Cheng et al., 2009; Z. N. Liu & Koyi, 2013), accretionary wedges (Wenk & Huhn, 2013), and fault-related folds (Hughes et al., 2014). It should be noted that this method can record the kinematic paths of the discrete elements. We have used this software to build a numerical model to compare with the analog model. The numerical model had the same initial geometry (Figure 4) and shortening rate as the analog models. The numerical model consisted of 6,285 circular particles, which were randomly distributed in a 120 cm × 5 cm rectangular region and had a bulk porosity of 20%. In the model, two discontinuities with friction coefficients of zero were generated in the model to simulate the pre-existing faults (QYF and HYF). The

Table 2
Experiment Parameters of the PFC Model

Layer no.	Stratum code	d (cm)	ρ (kg/m^3)	kn (N/m)	ks (N/m)	bn/bs (N)	μ	Mechanical property
Vb	Basal décollement horizon	0.8	2,200	1.5×10^7	0.5×10^7	8×10^4	0.2	Ductile
Lb	Basement-Z	2.2	2,600	3×10^9	1×10^9		0.7	Brittle
V1	Middle-Lower Cambrian	0.2	2,200	1.5×10^7	0.5×10^7	8×10^4	0.2	Ductile
L1	Upper Cambrian-Ordovician	0.4	2,600	3×10^9	1×10^9		0.7	Brittle
V2	Silurian	0.2	2,200	1.5×10^7	0.5×10^7	8×10^4	0.2	Ductile
L2	Silurian	0.2	2,600	3×10^9	1×10^9		0.7	Brittle
L3	Carboniferous-Permian	0.4	2,600	3×10^9	1×10^9		0.7	Brittle
V3	Middle-Lower Triassic	0.2	2,200	1.5×10^7	0.5×10^7	8×10^4	0.2	Ductile
L4	Upper Triassic-Jurassic	0.6	2,600	3×10^9	1×10^9		0.7	Brittle

Note. d-thickness, ρ-density, kn-particle normal stiffness, ks-particle shear stiffness, bn-normal contact bond strength, bs-shear contact bond strength, μ-coefficient of particle internal friction.

microscopic mechanical properties of the particles were divided into two categories: simulated glass-beads and silicone polymer. The macro-behavior reflects the bulk mechanical behavior and is controlled by the microscopic properties, including the particle size, particle stiffness, bond strengths, and particle friction coefficient (Table 2). During the simulation, we extracted the displacement parameter of the particles to investigate the lateral and vertical displacement characteristics of the model.

3.3. Low-Temperature Thermochronology

In this study, 11 outcrop samples were collected from the major thrust sheets for AFT, AHe, and ZHe analyses to reconstruct the Meso-Cenozoic tectonic-thermal evolution of the ESFTB (Table 3, and Figures 1b and 1c). AFTs are temperature sensitive between ~60 and ~125°C, which is referred to as the partial annealing zone (PAZ), on geological time scales (Fitzgerald & Malusà, 2018; Gleadow et al., 1986; Green et al., 1986; Ketcham

Table 3
Information of the Samples

Sample	Age	Lithology	Latitude (°N)	Longitude (°E)	Elevation (m)	Structural location	Reference
HY-1	J_2 (174–163 Ma)	Sandstone	30.3641	106.7806	389	Huayingshan anticline	
DZ-1	T_3 (235–201 Ma)	Sandstone	30.7755	107.1387	588	Huayingshan anticline	
DZ-2	J_2 (174–163 Ma)	Sandstone	30.7596	107.3200	466	Pubaoshan anticline	
JX-166	J (201–145 Ma)	Sandstone	30.2128	107.3334	388	Datianchi anticline	S. J. Li et al. (2011)
LP-1	J_3 (163–145 Ma)	Sandstone	30.6251	107.8850	395	Jinghuashan anticline	
RXZ-2	J_2 (174–163 Ma)	Sandstone	30.4700	108.0421	407	Dachigan anticline	
JX-168	J (201–145 Ma)	Sandstone	30.3123	108.0333	251	Dachigan anticline	S. J. Li et al. (2011)
Y42	J_2 (174–163 Ma)	Sandstone	29.9830	108.1629	206	Qiyueshan anticline	H. C. Shi et al. (2011)
QY-1	J_1 (201–174 Ma)	Sandstone	29.9602	108.3180	1,323	Qiyueshan anticline	
LC-2	J_2 (174–163 Ma)	Sandstone	30.1353	108.7849	1,300	Lichuan synclinorium	
WL-1	J_2 (174–163 Ma)	Sandstone	29.3606	107.7759	678	Jianshi anticlinorium	
X5	J (201–145 Ma)	Sandstone	30.2694	109.1451	1,310	Jianshi anticlinorium	Mei et al. (2010)
XF-1	J_1 (201–174 Ma)	Sandstone	29.4172	108.7954	490	Huaguoping synclinorium	
SZ-2	P_2 (272–259 Ma)	Sandstone	29.4489	110.1131	259	Sangzhi-Shimen synclinorium	
SZ-1	T_3 (235–201 Ma)	Sandstone	29.4398	110.1782	561	Sangzhi-Shimen synclinorium	
HC-38	S (444–419 Ma)	Sandstone	29.6444	111.0409	394	Xuefengshan thrust belt	S. J. Li et al. (2008)

et al., 2007). Within the temperature range of 30–90°C, which is referred to as the apatite partial retention zone (PRZ), the ^{4}He is partially retained (Reiners & Brandon, 2006; Wolf et al., 1998). The ZHe system is characterized by a PRZ of ~140–200°C (Reiners, 2005). The combination of AFT, AHe, and ZHe thermochronology data provides a powerful tool for constraining the thermal history of a sample between 30°C and 200°C.

The AFT analyses were performed at the China University of Petroleum, Beijing, following the procedures described by Chang et al. (2019b). The AFT ages of samples HY-1, DZ-1, DZ-2, WL-1, XF-1, LP-1, RXZ-2, QY-1, and SZ-1 were determined using the external detector method and ζ(zeta) calibration (Hurford & Green, 1983). The Trackkey software (Dunkl, 2002) was used to calculate the fission track ages based on a zeta-value of 246.9 ± 13.0 a/cm^2. The AFT ages of samples WL-1 and XF-1 were determined via laser ablation inductively coupled plasma mass spectrometry (LA-ICP-MS), following the procedures described by Cogné et al. (2020). For each sample, we analyzed the grains with polished surfaces parallel to the c-crystallographic axis. Horizontal confined track lengths and three etch pit diameter (D_{par}) were measured on each counted grain. D_{par} value is a proxy for resistance of apatite grains to annealing (Donelick et al., 2005). The RadialPlotter software identifies and extracts the component ages from mixed age populations (Vermeesch, 2012, 2018). For each sample, the grain age distributions were decomposed into discrete main age components using a mixture modeling algorithm and were manually selected after the fission track data were log transformed (Galibraith & Green, 1990). Furthermore, in addition to the AFT data set analyses of the current study, an additional five published AFT data sets were collected from the literature (S. J. Li et al., 2011; Mei et al., 2010; H. C. Shi et al., 2011).

The AHe ages of samples from Mesozoic sediments XF-1, WL-1, and HY-1 were determined at the University of Florida, following the procedures described by Chang et al. (2019a). Five apatite grains from each sample were tested. Published AHe data for samples from the same anticline and stratum as samples QY-1 (H. C. Shi et al., 2016) and DZ-2 (C. X. Li et al., 2021) were collected. ZHe analysis of zircon grains from samples DZ-1, DZ-2, LP-1, RXZ-2, QY-1, SZ-1, SZ-2, WL-1, and XF-1 was conducted at the University of Melbourne, following the procedures described by Gleadow et al. (2015). Details of experimental methods are presented in Supporting Information S1. We also collected ZHe data for samples from the same anticline and stratum as samples DZ-1, DZ-2, and HY-1 (C. X. Li et al., 2021).

3.4. Thermo-Kinematic Modeling

The analog models and thermochronology data were combined in a thermo-kinematic model by establishing a quantitative coupling relationship between the forward kinematic modeling and thermal modeling. In the analog models and DEM simulations, the geological time at a certain shortening magnitude (S, cm) was determined using the following equation:

$$t = 170 - S \times \frac{\Delta T}{30}, 0 \le S \le 30\,\text{cm} \quad (1)$$

where $\Delta T = 100$ Ma (from 170 to 70 Ma) of simulation with a shorting rate of 2.4 cm/hr. Based on the results of the analog models, we can determine the onset of deformation of the belt and the onset of cooling of the corresponding thermochronological samples. For example, the model-equivalent Jinghuashan anticline began to uplift when shortening of the analog model reached 21 cm. The model-equivalent geological time is 100 Ma at 21 cm shortening. We conclude that the onset time of model-equivalent Jinghuashan anticline is 100 Ma, and the onset of cooling of the sample LP-1 in the Jinghuashan anticline is 100 Ma. Based on Equation 1, 3-cm shortening in the analog models is equivalent to deformation taking place during 5 Ma in nature and 6 cm shortening in the model is equivalent to deformation taking place during 10 Ma in nature. Taking into account the experimental error, we set the error of ±10 Ma for the cooling onset of samples. We also recorded the trajectories of the particle elements during the deformation in the PFC2D modeling to constrain the kinematics of the thermochronological samples collected at the same structural positions. Since the geothermal gradient of the ESFTB was 30–35°C/km from the Jurassic to the Late Cretaceous (Q. Q. Feng et al., 2021; C. Q. Zhu et al., 2017), we converted the recorded kinematic uplift trajectories of the samples into temperature paths to constrain the Mesozoic thermal evolution.

We conducted inverse thermal-history modeling using the HeFTy v1.9.3 software (Ketcham et al., 2015). The multi-kinetic annealing model proposed by Ketcham et al. (2007) was selected for the AFT data, and the radiation damage accumulation and diffusion models created by Flowers et al. (2009) and Guenthner et al. (2013) were selected for the AHe and ZHe data, respectively. To avoid restricting the model in the identification of

possible temperature-time (*T-t*) paths, we set three *T-t* constraint windows for each model. The first constraint ranges were the stratigraphic age of sample and the surface temperatures of 20 ± 5°C. The second constraint encompassed the onset of cooling for the exhumation of the Mesozoic samples (±10 Ma on either side). For this constraint window, first, the temperature was set at 20–200°C to avoid restricting the model space and to capture the ZHe, AFT, and AHe data-driven *T-t*-paths with acceptable and good fits. Then, the range of temperature sensitivities was set as the new temperature window. The third constraint was set as 20 ± 5°C at the present time. We integrated the measured AFT data (track densities, D_{par}, and length measurements) and single-grain ZHe and/or AHe data in our models. For each sample, the HeFTy software tested at least 10,000 random *T-t* paths and calculated the modeled ZHe, AHe, and AFT data for each path, which was compared with the measured input data. We selected as many individual grains as possible, with the prerequisites that (a) more than one grain was collected and (b) statistically acceptable *t-T* pathways were acquired. An estimated goodness-of-fit (GOF) parameter was used to reflect how well the modeled data fit the measured values. In the program, the *t-T* paths were defined as acceptable when the GOF was >0.05 and as good when the GOF was >0.5. The best-fit and weighted mean paths are shown by the yellow and blue lines in Figures 2b and 9, respectively. Cooling histories of samples were reconstructed by two different methods. In scenario A, the individual samples were separately simulated using the AFT, AHe, and ZHe ages. In scenario B, the individual samples were simulated using only the AFT and ZHe ages. Compared with the inversion modeling results in scenario A, the cooling histories for scenario B provide a less reasonable cooling process during the Cenozoic and are not discussed here.

3.5. Cross-Section Restoration

To evaluate the data and quantitatively analyze the structural evolution, 2D sequential restoration was conducted using algorithms to simulate the reversal of the geological processes. We constructed a geological cross-section (A-A') traversing the Jiangnan-Xuefengshan orogen, the thick-skinned domain, the transition zone, the thin-skinned domain, and the central Sichuan Basin from southeast to northwest (Figure 1c). Based on the above thermo-kinematic analysis, the cross-section restoration was conducted using a combination of two kinematic methods implemented as algorithms in the Move 2D modeling software. The fault-parallel flow method (Egan et al., 1999) has been used for modeling hanging-wall deformation which occurs between beds over the fault plane. In fault-parallel flow method, horizon movement is "layer parallel" and particles within the hanging wall translate parallel to the fault surface along flow paths (Herrero-Barbero et al., 2020). For restorations that require adjusting the geometry of the hanging-wall sequence due to the presence of a previous fold, the trishear method (Allmendinger, 1998) has been used locally. Exhumation histories reconstructed using the thermo-kinematic models were used to calibrate decompaction calculations and back stripping. We used the restored cross sections and the kinematic constraints on the timing of the activity to estimate the average shortening ratio of each thrust sheet across the pro- and retro-wedges of the ESFTB. The minimum overall shortening ratio for a given period was derived by summing the shortening ratios of all of the unlinked structures that were active during that period. The cross-section restoration allowed us to assess the structural evolution of the ESFTB and to quantify the shortening and dip-slip motion during the Mesozoic-Cenozoic.

4. Results

4.1. Mesozoic Kinematic Restoration

Similar to the tectonic evolution of the ESFTB, during the modeled Mesozoic time-equivalent, the models consisted of northwestward thrusts evolving from the Late Jurassic to Cretaceous (Figure 5). With progressive shortening, at 15% bulk shortening, a series of decollement folds and fault-propagation folds formed progressively in an in-sequence manner (Figures 5a–5c), forming prototype of the thick-skinned domain. Decollement fault F1 initiated above the basal décollement and developed into a fault-bend fold with a fault ramp cutting upward resulting in the formation of a decollement-buckle fold in the hanging wall. Flat-ramp type faults F4 and F5 were sequentially formed along the viscous layer V3 with two fault-propagation folds. Continued shortening resulted in formation of basal decollement faults F9 and F10 and another decollement-buckle fold. The pre-existing fault (F6 in Figure 5) was resurrected after 10% of shortening and began to accommodate a large amount of the shortening. As shortening proceeded, the formation of faults F22, F28-30 and fault-propagation folds along the viscous décollement V2 produced forward-propagating imbricate thrusts (Figure 5e). Simultaneously, the transition zone is transformed from decollement fold to fault-bend fold, which produced a passive

10.1029/2022TC007630

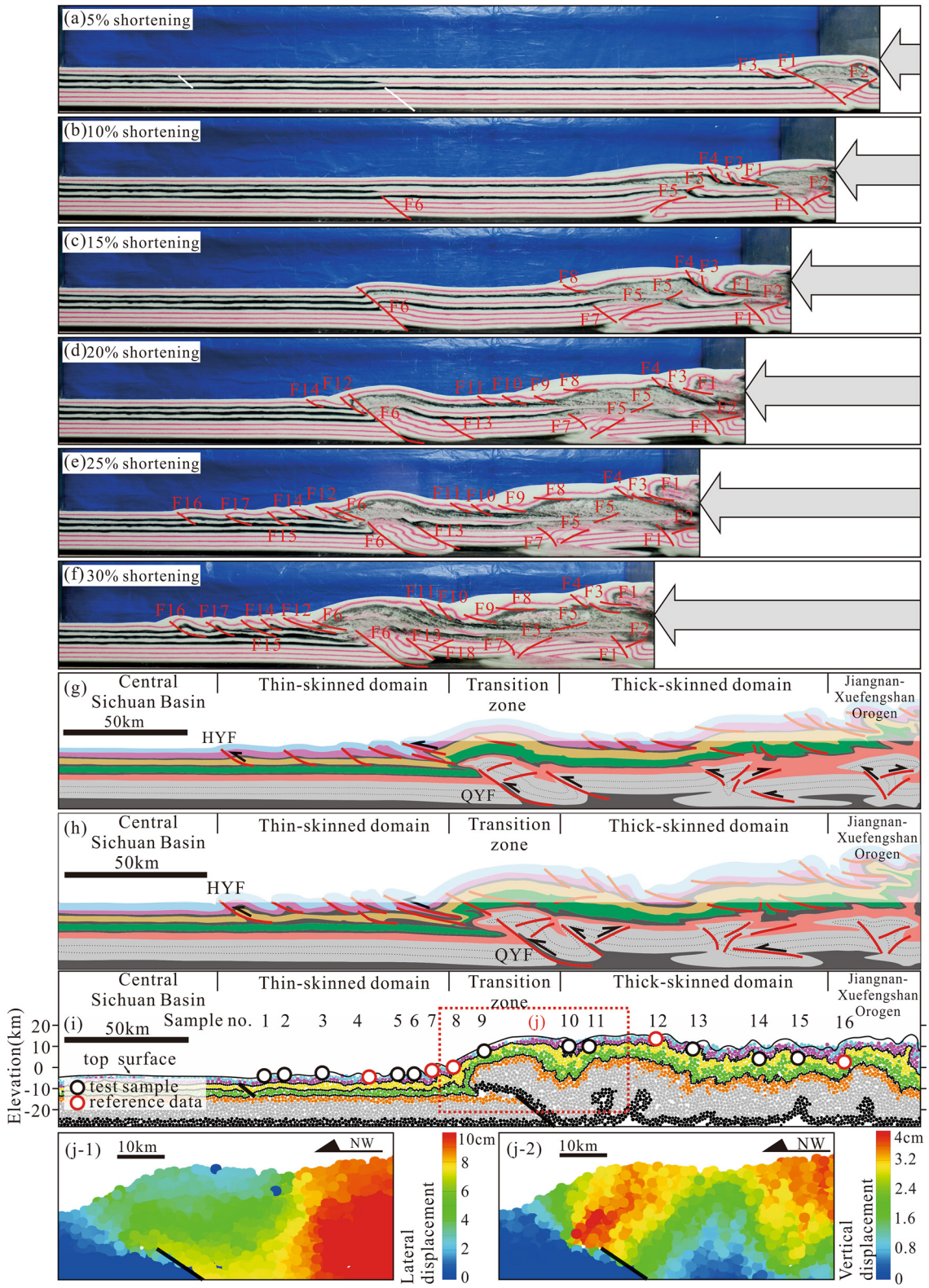

Figure 5. (a–f) Sequential sidewall views of the analog model. White lines represent the initial locations of pre-existing faults equivalent to Huayingshan fault and Qiyueshan fault. *F* is thrust faults which are numbered in the order of their formation. The tectonic pattern after 25% (g) and 30% (h) of shortening are interpreted based on geological scale and the eroded part is displayed in light color. (i) Particle flow code (PFC2D) modeling result after 25% of shortening. Numbers 1–16 represent the constraint points that match the samples shown in Figure 1c. (j) Lateral (j-1) and vertical (j-2) displacement fields of the transition zone in the PFC2D modeling result.

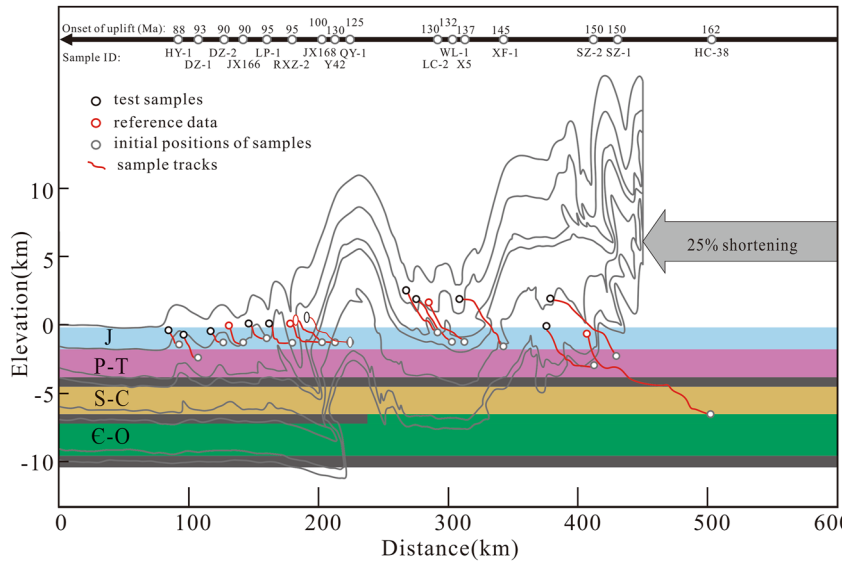

Figure 6. Sample tracks after 25% of shortening shown with corresponding onset of uplift. The black lines show model profile after 25% of shortening.

duplex with roof thrust along the viscous layer V1 and floor thrust along the basal décollement. After 25% of shortening, a total of five fault-propagation folds formed between the pre-existing faults (Figures 5e and 5g), and they became steeper and tighter with shortening (Figures 5f and 5h). Simultaneously, the configuration of the thick-skinned domain gradually transitioned to broader anticlinoriums and tighter synclinoriums. After 30% shortening, the sidewall view (i.e., profile) of the model (Figure 5h) showed similar structural configuration as that of the seismic profiles (Figure 1c), including the division of tectonic regions, the frequency of narrow anticlines and narrow synclines, and relative stratigraphic outcrops.

Based on the results of analog models, we conducted a corresponding numerical simulation using the PFC2D software. After 25% shortening (Figures 5i and 5j), the results are generally consistent both with the interpreted seismic profile (Figure 1c) and results of the analog model (Figures 5e and 5g). Three box-folds were formed in sequence to the southeast of the model QYF. Displacement fields of the model showed that differential uplift occurred in the thrust domain. For example, lateral displacement decreased from southeast to northwest, while vertical displacement increased in the transition zone (model equivalent of the Qiyueshan anticline) (Figure 5k). These results indicate that the particles uplifted earlier with more lateral displacement to the northwest of the transition zone, and particles uplifted later with less lateral displacement in the southeastern part of the area. Finally, the onset of the uplift occurred progressively earlier from southeast to northwest in the transition zone. Trajectories of particle elements in the model were recorded as the Mesozoic kinematic constraints for the thermochronological samples collected at the corresponding structural positions (Figure 5i). We simultaneously compared the vertical displacement of monitored particles to the results of the analog model (Figure 6). Under a constant shortening rate, particle trajectories are complex. Each particle moves both laterally and vertically; that is, as the particles are pushed forwards by the backstop, they also move upwards as the layers thicken tectonically by layer-parallel thickening or by duplication due to imbrication. Generally, the closer the particle is to the model-equivalent Jiangnan-Xuefengshan orogen, the greater the lateral displacement. The particle (equivalent of sample HC-38) shows as much as 90 km of lateral displacement.

Published thermochronological data (X. M. Li & Shan, 2011; Richardson et al., 2008; C. B. Shen et al., 2009) indicate that the samples from Jurassic strata near to the core of the narrow anticlines experienced a rapid cooling (30–50°C decrease) during the Early-Late Cretaceous. This cooling is approximately one-third to one-half of total cooling since the Early Cretaceous (~100°C) (Figure 3). Simultaneously, results of the analog model show that the uplift height of the narrow-anticline domain at 25% of shortening is also one-third to one-half of that at 30% shortening. Therefore, we speculate that the model configuration after 25% (30 cm) of shortening (Figure 5g) represents the tectonic geometry of the ESFTB after the rapid cooling in the Mesozoic (from ~170 to ~70 Ma). Since we adopted a constant shortening rate, the initial uplift time of the samples could be

Table 4
Measured Apatite Fission Track Data by the External Detector Method

Sample ID	No. grains	ρ_s (10^5/cm^2) (N_s)	ρ_i (10^5/cm^2) (N_i)	ρ_d (10^5/cm^2) (N_d)	$P(\chi^2)$ (%)	U (ppm)	Pooled age ± 1σ (Ma)	Mean track length ±SD (μm) (no. lengths)	Mean D_{par} (μm)
HY-1	21	2.377 (569)	5.69 (1.362)	14.628 (17,488)	10.41	9.04	75.7 ± 6.2	12.15 ± 2.23 (54)	2.11
DZ-1	26	4.851 (343)	11.952 (845)	16.754 (17,488)	42.11	17.56	80.2 ± 6.0	12.41 ± 2.11 (55)	1.95
DZ-2	22	5.7 (268)	16.42 (772)	16.573 (17,488)	83.42	17.88	70.6 ± 6.3	12.04 ± 2.16 (44)	2.05
LP-1	37	7.764 (936)	19.244 (2,320)	16.328 (17,488)	37.42	17.54	81.0 ± 5.4	12.04 ± 1.88 (110)	1.86
RXZ-2	32	1.875 (782)	5.245 (2,186)	16.174 (17,488)	12.65	5.22	71.8 ± 5.0	12.67 ± 1.81 (77)	1.88
QY-1	36	10.386 (743)	22.421 (1,604)	15.401 (17,488)	45.32	23.24	87.5 ± 6.1	12.49 ± 1.62 (105)	1.86
SZ-1	41	15.872 (1,295)	29.661 (2,420)	14.783 (17,488)	62.4	31.4	96.9 ± 6.2	11.71 ± 1.74 (117)	1.86
LC-2	22	4.494 (430)	10.106 (967)	15.246 (17,488)	90.11	16.13	83.2 ± 6.6	13.99 ± 1.14 (46)	2.30

Note. ρ_s, ρ_i, and ρ_d are the density of spontaneous, induce, and dosimeter tracks, respectively. N_s, N_i, and N_d are the number of spontaneous, induce and dosimeter tracks, respectively. $P(\chi^2)$ is chi-square probability. AFT ages were calculated with Trackkey (Dunkl, 2002) by using a zeta-value of 246.9 ± 13.0. MTL is Mean track length. SD is the standard deviation of measured confined track lengths. n and N are the number of tested grains and tracks, respectively. Three D_{par} value were measured for each grain.

easily calculated based on the entire duration of deformation (~170–70 Ma). Both the thin-skinned and thick-skinned domains exhibited northwestward propagation of thrust imbricates. Based on the analog modeling results, the onsets of the model-equivalent thrusts of the cross-section (A-A') were determined. Formation of the Huayingshan, Pubaoshan, Datianchi, Jinghuashan, and Dachigan anticlines began at 93, 90, 90, 95, and 100 Ma, respectively. The Qiyueshan anticline, Jianshi anticlinorium, Huaguoping synclinorium, and Sangzhi-Shimen synclinorium began to develop at 130, 137, 145, and 150 Ma, respectively.

4.2. Thermochronological Ages

The AFT ages of samples of the current study range from 70.6 ± 6.3 to 98.0 ± 12.7 Ma (Tables 4 and 5). The mean fission track lengths range from 11.12 to 13.99 μm, with standard deviations of ±1.62–2.23 μm. The mean D_{par} values for all the samples range between 1.78 and 2.30 μm (Tables 4 and 5). Nine samples pass the chi-square test, and their pooled ages are reported. For sample XF-1, the central age is reported (Table 5). We plotted the single-grain AFT ages for each sample on a radial plot using the RadialPlotter software (Vermeesch, 2018) (Figure 7). Details of single-grain AFT ages are presented in Supporting Information S1. The single-grain AFT ages of all the samples are significantly younger than their stratigraphic ages, which indicates that these samples were completely reset. The AFT single crystal ages of nine samples pass the chi-square test, and they can be considered to belong to the same population. Sample XF-1 fails the chi-square test, and the radial plot suggests a single age population (107.7 ± 6.9 Ma). The AFT data for some of the samples (HY-1 and XH-1) exhibit a large dispersion. Additionally, we also observed a generally wide range of D_{par} values. This indicates variations in the annealing kinetics, which likely contributed to the high age dispersion. The D_{par} is an indicator of a grain's resistance to annealing during its residence in the PAZ, where values of >1.75 μm indicate more resistance than values of <1.75 μm (Carlson et al., 1999). The overall low uranium concentration and the prolonged thermal history within the upper 5 km of the crust are the main reasons for the observed intra-sample age dispersion (Fraser et al., 2021). This age dispersion can be exploited by thermal modeling. Confined track lengths are not typically measured in detrital samples because individual detrital grains cannot be assumed to represent the sample's thermal history if there are multiple single-grain age peaks. However, when there is only one age peak in a sample, it is possible to define the thermal history by determining the confined track length distribution of the sample, and whether the sample is composed of grains that have all rapidly cooled and/or the age peak represents a simple rapid cooling/exhumation event. The track lengths of all of the samples are used for the thermal history modeling. The bimodal track length distribution of sample HY-1 suggests a two-stage cooling history (Gleadow et al., 2002). The track length distribution of sample LC-2, exhibits an undisturbed basement type distribution (Gleadow et al., 2002), with longer mean length (13.99 ± 1.14 μm), indicating rapid cooling through the AFT PAZ. The track lengths for other samples exhibit skewed distributions (Gleadow et al., 2002), with relatively short mean lengths (11.12 ± 2.02–12.67 ± 1.81 μm), suggesting a relatively slow cooling through the AFT PAZ.

A total of 20 apatite grains from five samples were analyzed and were found to have single-grain ages ranging from 17.1 ± 0.9 to 84.3 ± 4.4 Ma (Table 6). One datum was rejected because it had a significantly higher effective uranium (eU) content and younger age (WL-1c). Four single ages (WL-1e, XF-1b, XF-1d, and HY-1b) were not included in the inverse models because they were significantly older or younger than all of the other ages in the data set. Overall, the single-grain ages for each sample are widely dispersed and the weighted mean ages range from 20.4 ± 4.89 to 58.7 ± 16.65 Ma, with a standard deviation of >20%. The single grain AHe ages are characterized by obvious dispersion, which can be caused by various factors, including U- and Th-rich microinclusions,

Table 5
Measured Apatite Fission Track Data by the LA-ICP-MS

Sample	Gains	ρ_s (10^5/cm^2) (N_s)	U (ppm)	ζ_{ICP} (yr cm^2)	$2\sigma\zeta_{ICP}$	P (χ^2)	AFT age ± 2σ (Ma)	MTL ±SD (μm) (N)	D_{par} (μm)
WL-1	34	12.170 (885)	28.15	0.531	0.058	0.63	90.9 ± 11.7	11.63 ± 1.80 (102)	1.90
XF-1	32	10.720 (1,162)	24.85	0.528	0.060	0.00	98.0 ± 12.7	11.12 ± 2.02 (77)	1.78

Note. ζ_{ICP} is the zeta factor for the ICP-MS.

radiation damage, grain size, U-Th zoning, cooling rate, chemical influences, helium addition from an external source, and grain breakage. In general, larger apatite grains and those with more radiation damage are more resistant to helium loss through diffusion, and therefore, they have a higher closure temperature and older AHe ages compared to the grains that are smaller and/or have less radiation damage (Farley, 2002; Flowers et al., 2009; Willett et al., 2017). The AHe ages from sample XF-1 are weakly positively correlated with the eU content but are not correlated with the crystal radius (Figures 8a and 8c). The other four samples don't exhibit positive correlations between the AHe ages and the eU contents and crystal radius (Figures 8b and 8d).

We obtained 45 ZHe ages for 11 samples (Table 7). One datum was rejected because of a significant amount of ^{4}He (HY-1c). Another datum was rejected because the age is significantly younger than the AFT age (DZ-2d). The single ZHe ages of sample DZ-2 range from 184.6 ± 2.2 to 306.6 ± 4.0 Ma and are significantly older than the depositional ages, suggesting that the sample was not reset. Six samples (WL-1, QY-1, DZ-1, RXZ-2, XF-1, SZ-1, and HY-1) yield ZHe ages of some grains older than their depositional ages, indicating that these samples were partially reset. The ZHe ages of three samples (LC-2, LP-1, and SZ-2) are all younger than their depositional ages. The samples were separated into two groups according to their ZHe ages. In Group 1, which consists of

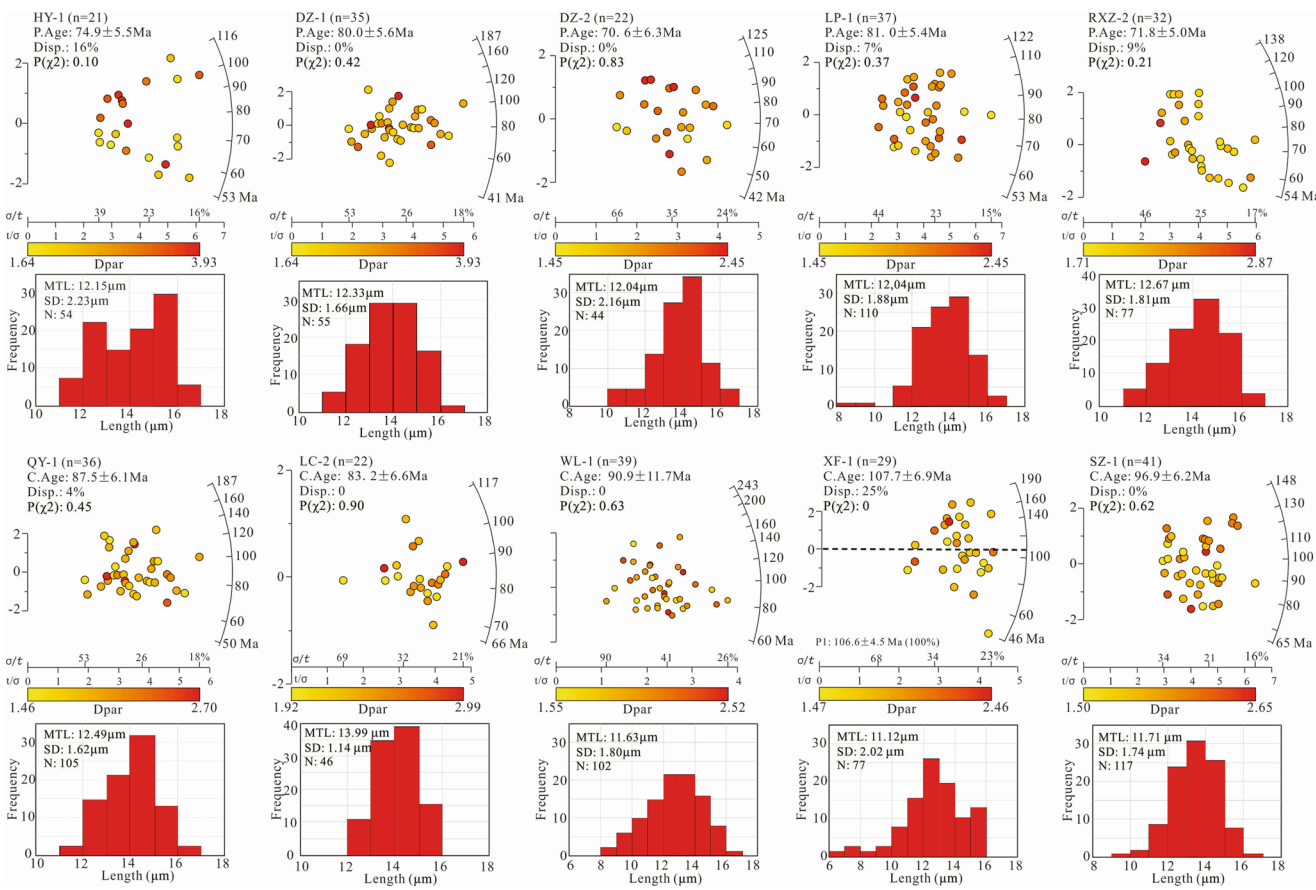

Figure 7. Radial plots of single-grain apatite fission track ages for all samples using RadialPlotter (Vermeesch, 2018). C. Age-Central age; P. Age-Pool age; Disp.-Dispersion; MTL-Mean track length; SD-the standard deviation of measured confined track lengths. Dashed black line represent the peak ages.

Table 6
AHe Data

Sample	Radius (μm)	Mass (μg)	^{4}He (nmol g^{-1})	U (ppm)	Th (ppm)	Sm (ppm)	eU (ppm)	Raw age (Ma)	F_T	Corrected age (±1σ) (Ma)
WL-1a	39.1	1.4	2.4	4.2	63.6	69.3	19.2	22.9	0.610	37.5 ± 2.0
WL-1b	44	1.9	2.9	4.2	54.6	156.7	17	30.5	0.650	47.0 ± 2.5
~~WL-1c~~	~~38.8~~	~~1.1~~	~~9~~	~~42.1~~	~~103.0~~	~~210.4~~	~~66.3~~	25.2	~~0.630~~	~~39.9 ± 2.1~~
WL-1d	38.4	1.3	1.7	3.9	28.3	144.5	10.5	29.6	0.610	48.5 ± 2.6
WL-1e[a]	36.7	0.9	0.6	2.8	34.8	93.1	11	10.3	0.590	17.4 ± 1.0
								Mean age ± SD (SD%)		37.6 ± 12.40 Ma (33.0)
XF-1a	51.5	1.9	2.1	10.8	10.5	79.7	13.2	29.2	0.716	40.8 ± 2.2
XF-1b[a]	47.7	1.9	3.9	8.9	22.9	168.3	14.3	49.6	0.688	72.1 ± 3.8
XF-1c	43.4	1.4	6.2	20.9	57.0	91.7	34.3	33.4	0.660	50.6 ± 2.6
XF-1d[a]	51.3	3.3	18.1	45.7	40.1	94.2	55.1	60.3	0.715	84.3 ± 4.4
XF-1e	48.8	2.4	2.1	10.7	4.5	43.8	11.7	32.3	0.705	45.8 ± 2.9
								Mean age ± SD (SD%)		58.7 ± 16.65 Ma (28.4)
HY-1a	46.2	1.5	4.1	24.9	173.2	245.3	65.6	11.6	0.670	17.3 ± 0.9
HY-1b[a]	40.3	0.9	4.6	12.6	144.8	188.3	46.6	17.9	0.622	28.8 ± 1.6
HY-1c	46.1	1.6	3.6	7.6	196.5	153.2	53.8	12.1	0.659	18.4 ± 1.0
HY-1d	55.7	2.5	3.8	7.5	212.6	233.7	57.5	12.2	0.713	17.1 ± 0.9
								Mean age ± SD (SD%)		20.4 ± 4.89 Ma (24.0)
QY-1a	39.8	1.7	2	6.6	20.1	29.1	11.3	31.4	0.620	50.6 ± 3.0
QY-1b	38.2	1.3	1.9	5.8	26.6	16.9	12.1	28.6	0.600	47.6 ± 2.9
QY-1c	42.3	1.7	1.5	12.2	9.3	28.7	14.4	18.7	0.650	28.8 ± 1.7
								Mean age ± SD (SD%)		42.33 ± 9.65 Ma (22.8)
DZ-2a	29.2	_	11	94.7	29.0	_	101.5	_	_	37.0 ± 1.0
DZ-2b	46.7	_	7.9	22.3	83.0	_	41.8	_	_	50.4 ± 0.7
DZ-2c	36	_	5.3	47.7	24.3	_	53.4	_	_	29.5 ± 0.7
								Mean age ± SD (SD%)		38.97 ± 8.64 Ma (22.2)

Note. eU: Effective uranium concentration, calculated from the contents of U and Th, eU = U + 0.235Th (Flowers et al., 2007). The AHe data of sample QY-1 are collected from the sample Y21 in H. C. Shi et al. (2016). The AHe data of sample DZ-2 are collected from the sample HY24 in C. X. Li et al. (2021). SD: standard deviation.

[a]Grains with significantly younger or older AHe ages have not been included in the inverse models. ~~Strikethrough~~, Underlined values are removed from the data set.

samples XF-1, QY-1, LP-1, RXZ-2, SZ-1, and LC-2, the single-grain ages for each sample are widely dispersed, with mean ages ranging from 153.0 ± 17.8 to 248.7 ± 44.5 Ma and a low SD of <20%. Group 2, which consists of the remaining five samples (WL-1, DZ-1, DZ-2, SZ-2, and HY), has more dispersed ZHe ages. These samples yield ZHe ages of 220.6 ± 45.5 to 250.1 ± 57.9 Ma, with a high SD of >20%. In general, the thermochronological ages of the partially reset detrital zircon grains exhibit several types of ZHe age-eU correlations due to the variations in the pre-depositional (inherited) ages, radiation-damage-induced He diffusion kinetics, and grain sizes, as well as other factors. A larger grain size results in a higher closure temperature. Radiation damage can hinder the diffusion of helium (Flowers et al., 2009) or accelerate the diffusion of helium (Guenthner et al., 2013). We plotted the single-grain ages against the eU content and the spherical radius (Figures 8e–8j). Sample LP-1 exhibits a positive correlation between the crystal radius and ZHe ages, while sample SZ-1 exhibits a negative correlation between the crystal radius and ZHe ages (Figure 8e), but both samples lack any correlation between the eU contents and ZHe ages (Figure 8h). The dispersion of the ZHe ages of samples LP-1 and SZ-1 results from the grain-size variation. Samples RXZ-2 and LC-2 exhibit a general negative correlation between the eU content and ZHe ages and a positive correlation the age dispersion of samples RXZ-2 and LC-2. For samples WL-1, DZ-1, and SZ-2, a negative correlation between the eU content and ZHe ages is observed (Figure 8g), whereas there is no correlation between the ZHe ages and crystal radius (Figure 8j). Samples XF-1, QY-1, DZ-2, and HY-1

10.1029/2022TC007630

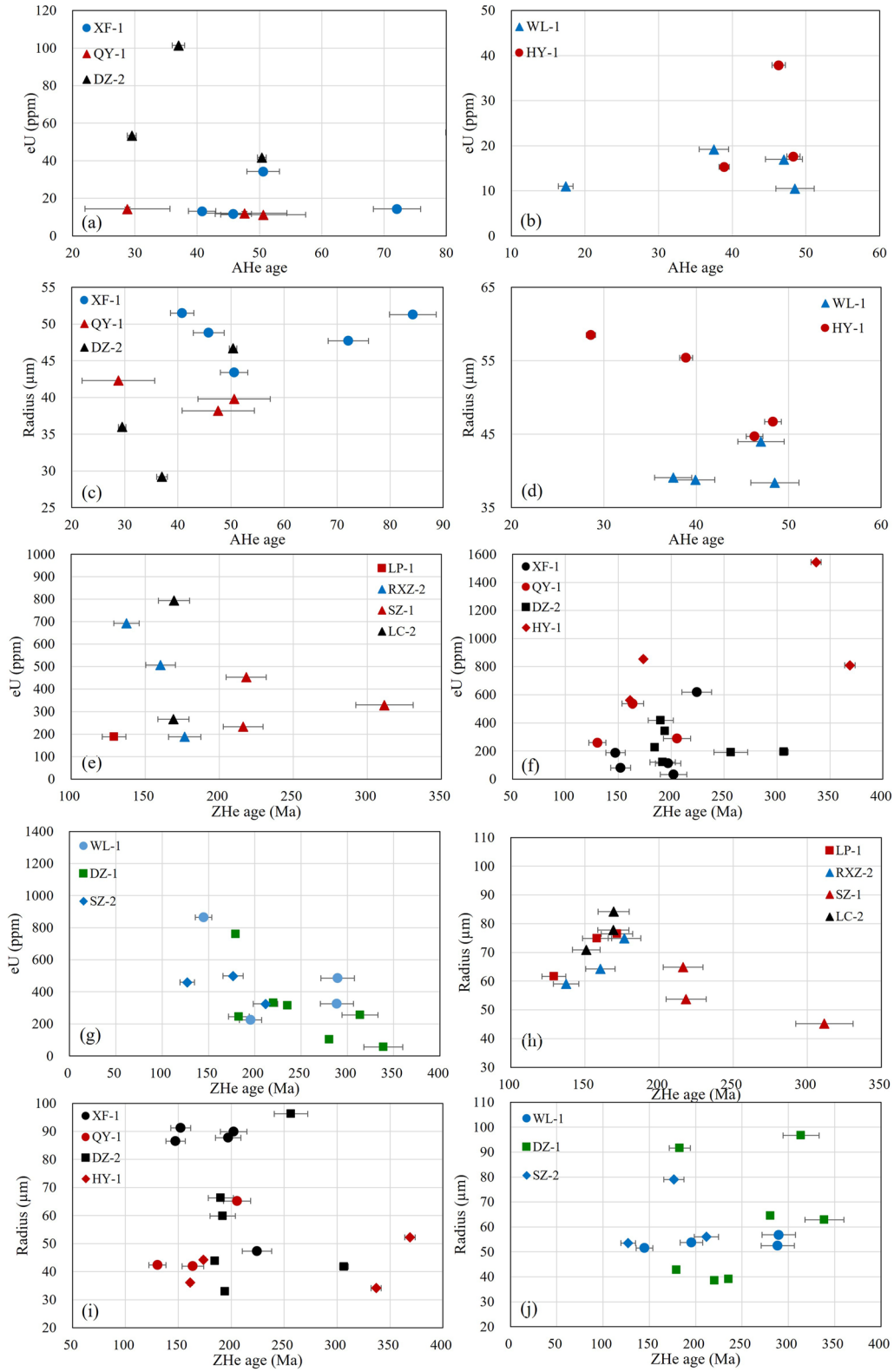

Figure 8. (a, b) Correlation of AHe single grain age with effective uranium (eU). (c, d) Correlation of AHe single grain age with radius. (e–g) Correlation of ZHe single grain age with eU. (h–j) Correlation of ZHe single grain age with radius.

Table 7
ZHe Data

Sample	Radius (μm)	Mass (μg)	^{4}He (nmol g^{-1})	U (ppm)	Th (ppm)	eU (ppm)	Raw age (Ma)	FT	Corrected age (±1σ) (Ma)
WL-1a[a]	56.8	3.74	65.5	430.9	228.6	484.6	217.3	0.751	289.6 ± 18.0
WL-1b[a]	52.5	3.14	36.9	269	242.5	325.9	214.0	0.741	288.6 ± 17.9
WL-1d	51.5	4.93	75.9	774.5	382.3	864.3	111.0	0.767	144.7 ± 9.0
WL-1e[a]	53.7	17.59	95.6	196.3	120.4	224.6	169.2	0.866	195.4 ± 12.1
							Mean age ± SD (SD%)		229.6 ± 62.2 Ma (27.1)
XF-1a[a]	87.7	15.58	42.6	100.2	50.1	112	167.3	0.848	197.2 ± 12.0
XF-1b	91.2	13.70	20.7	69.3	47.3	80.5	129.3	0.849	152.2 ± 9.4
XF-1c	86.5	12.55	42.8	173.1	61.3	187.5	124.6	0.845	147.4 ± 9.1
XF-1d[a]	89.9	16.36	13.4	28.3	18.9	32.8	173.5	0.858	202.3 ± 12.5
XF-1e[a]	47.3	1.80	31	542.3	320	617.5	160.7	0.717	224.2 ± 13.9
							Mean age ± SD (SD%)		184.7 ± 29.9 Ma (16.2)
QY-1a[a]	65.2	8.79	64.8	271.5	75.2	289.2	166.4	0.810	205.6 ± 12.7
QY-1b	42.4	2.10	8.7	225.7	143.5	259.4	90.5	0.694	130.3 ± 8.1
QY-1c	41.9	2.28	24.7	479.2	242.2	536.1	110.8	0.677	163.7 ± 10.1
							Mean age ± SD (SD%)		166.5 ± 30.8 Ma (18.5)
DZ-1a	91.6	21.90	121.2	197.4	203.2	245.2	156.6	0.857	182.8 ± 11.3
DZ-1b[a]	62.9	11.63	27.5	45.4	43.7	55.7	266.0	0.785	338.9 ± 21.0
DZ-1c[a]	96.6	22.87	229.5	220.6	148.9	255.6	269.1	0.858	313.7 ± 19.4
DZ-1d	38.6	_	274	264.4	283.1	330.9	_	_	220.2 ± 2.6
DZ-1e	42.8	_	536.3	705.9	234.4	761	_	_	179.4 ± 2.4
DZ-1f[a]	64.4	_	129.8	94.3	40.6	103.8	_	_	280.6 ± 3.6
DZ-1g	39.1	_	282	264.8	215.2	315.4	_	_	235.4 ± 2.9
							Mean age ± SD (SD%)		250.1 ± 57.9 Ma (23.2)
DZ-2a[a]	96.2	22.59	138	165	112.3	191.4	221.4	0.863	256.4 ± 15.9
DZ-2b[a]	66.2	13.35	131.4	376.4	178.9	418.5	153.8	0.809	190.1 ± 11.8
DZ-2c[a]	59.8	7.66	21.9	104.7	66.3	120.3	149.2	0.778	191.9 ± 11.9
~~DZ-2d~~	~~41.1~~	_	~~24.5~~	~~147.6~~	~~105.2~~	~~172.3~~	_	_	~~37.3 ± 0.5~~
DZ-2e[a]	43.8	_	164.2	171	235.8	226.5	_	_	184.6 ± 2.2
DZ-2f[a]	33	_	232.7	271.5	305.3	343.3	_	_	194.0 ± 2.3
DZ-2g[a]	41.8	_	234.1	172.9	90.3	194.1	_	_	306.6 ± 4.0
							Mean age ± SD (SD%)		220.6 ± 45.5 Ma (20.6)
LP-1a[a]	76.4	10.18	230.2	986.4	342.1	1,066.8	142.1	0.828	171.7 ± 10.6
LP-1b	61.7	8.90	26.7	180	37	188.7	102.4	0.793	129.1 ± 8.0
LP-1c	74.9	11.98	279.1	1,084.5	465.2	1,193.8	131.0	0.828	158.2 ± 9.8
							Mean age ± SD (SD%)		153.0 ± 17.8 Ma (11.6)
RXZ-2a	59	6.93	81.2	677.1	66.6	692.7	107.7	0.784	137.4 ± 8.5
RXZ-2b[a]	74.9	14.20	58.3	171.4	70.8	188	146.6	0.829	176.7 ± 11.0
RXZ-2c	64.3	8.12	81.5	462.2	190.6	507	128.4	0.800	160.5 ± 9.9
							Mean age ± SD (SD%)		158.2 ± 16.1 Ma (10.2)
SZ-1a[a]	45.2	3.06	39.2	287.6	175.4	328.8	222.6		0.714
SZ-1b	53.7	5.25	64.4	426.4	111.3	452.6	163.5		0.749
SZ-1c	64.9	6.74	42.1	188.3	191	233.2	170.7		0.789
							Mean age ± SD (SD%)		248.7 ± 44.5 Ma (17.9)

Table 7
Continued

Sample	Radius (μm)	Mass (μg)	^{4}He (nmol g^{-1})	U (ppm)	Th (ppm)	eU (ppm)	Raw age (Ma)	FT	Corrected age (±1σ) (Ma)
SZ-2a	79.1	11.30	123.1	434.2	274.9	498.8	146.6	0.830	176.6 ± 10.9
SZ-2b	56	8.00	67.8	304.1	87.1	324.6	165.0	0.780	211.6 ± 13.1
SZ-2c	53.5	5.00	35.8	433	111.7	459.2	96.6	0.760	127.1 ± 7.9
							Mean age ± SD(SD%)		171.8 ± 34.7 Ma (20.2)
LC-2a	77.8	15.26	85	234.4	136.9	266.6	140.4	0.830	169.2 ± 10.5
LC-2b	84.2	18.11	300.7	709	360	793.5	143.3	0.846	169.4 ± 10.5
LC-2c	70.9	12.48	320.7	1,256	527.1	1,379.9	124.6	0.825	151.0 ± 9.4
							Mean age ± SD(SD%)		163.2 ± 8.6 Ma (5.3)
HY-1a	36.1	_	330	508.3	216.5	559.2	_	_	161.1 ± 2.2
HY-1b	44.3	_	585.6	736.5	500.3	854	_	_	173.7 ± 2.3
~~HY-1c~~[a]	~~34.1~~	_	~~1,892.1~~	~~1,452.8~~	~~386.5~~	~~1,543.6~~	_	_	~~337.0 ± 4.8~~
HY-1d[a]	52.2	_	1,267	699	467.9	808.9	_	_	368.8 ± 4.9
							Mean age ± SD(SD%)		234.5 ± 95.1 Ma (40.6)

Note. The ZHe data of grains DZ-1d-e are collected from the sample HX06. Data of grains DZ-2d-g are collected from the sample HY24, and the data of sample HY-1 are collected from the sample HX02 (C. X. Li et al., 2021). SD: standard deviation.

[a]Grains with significantly younger or older ZHe ages have not been included in the inverse models. ~~Strikethrough~~, Underlined values removed from the data set.

don't exhibit a correlation between the ZHe ages and the eU contents and the crystal radius (Figures 8f and 8i). A combination of several factors, including the U-Th zonation, grain-size variation, invisible fluid inclusions, and/or radiation damage results in the age dispersion of these samples.

4.3. Thermo-Kinematic Models

Thermal history modeling was conducted for all 11 samples, and five published thermal history models were collected from previous studies by Mei et al. (2010), S. J. Li et al. (2011), and H. C. Shi et al. (2011) (Figure 9). As the pre-Mesozoic thermal histories remain highly uncertain, they are not discussed and presented here. In our interpretation of the thermal history modeling results, we considered the envelope of all of the good *T*-*t* paths, the best-fit path and the weighted mean path to fit the observed data. The inversion modeling results suggest that the ESFTB experienced northwestward deformation during the Mesozoic-Cenozoic. Samples SZ-1 and SZ-2 from the Sangzhi-Shimen synclinorium, sample XF-1 from the Huaguoping synclinorium, and samples WL-1 and X5 from Jianshi anticlinorium show that exhumation started at 150, 148, and 135 Ma, respectively. The thermal histories of samples LC-2, QY-1, and Y42 show that the QYF became active at 130 Ma, and fault-related folding developed in the transition area in the period between 130 and 100 Ma. The thin-skinned domain formed later during 100–70 Ma. The onset of the cooling of samples RXZ-2 and JX-168 in the Dachigan anticline, sample LP-1 in the Jinghuashan anticline, and sample JX-166 in the Datianchi anticline occurred at 100, 100, and 90 Ma, respectively. Exhumation in the Pubaoshan anticline (sample DZ-2) and Huayingshan anticline (samples DZ-1 and HY-1) started at 88 and 100 Ma, respectively.

We defined the cooling process as slow when the cooling rate was lower than 1.0°C/Ma; otherwise, it was defined as rapid cooling. The thermal history of sample SZ-1 was characterized by a rapid cooling rate of 1.57°C/Ma during 150–115 Ma, a slow cooling rate of 0.23°C/Ma until 20 Ma, and finally an accelerated cooling rate of 2.15°C/Ma. No reasonable cooling process was identified for sample SZ-2, but the thermal histories constrained by the single-ZHe ages may record the onset of cooling at 150 Ma from a maximum temperature 175°C. Samples XF-1 and WL-1 cooled rapidly during 135–110 and 148–100 Ma, with cooling rates of 2.80 and 1.77°C/Ma, respectively. Since ca. 110 Ma, these two samples have cooled slowly, with cooling rates of 0.64 and 0.60°C/Ma, respectively. Sample LC-2 was buried and heated to a maximum temperature of 125°C at 130 Ma, followed by a rapid cooling stage at a rate of 1.20°C/Ma until 80 Ma, slow cooling at a rate of 0.17°C/Ma until 20 Ma, and finally accelerated cooling at a rate of 1.75°C/Ma. Sample QY-1 was collected from the transition zone. It cooled rapidly at a rate of 1.83°C/Ma during 130–100 Ma and then cooled slowly at a rate of 0.70°C/Ma from 100 Ma to

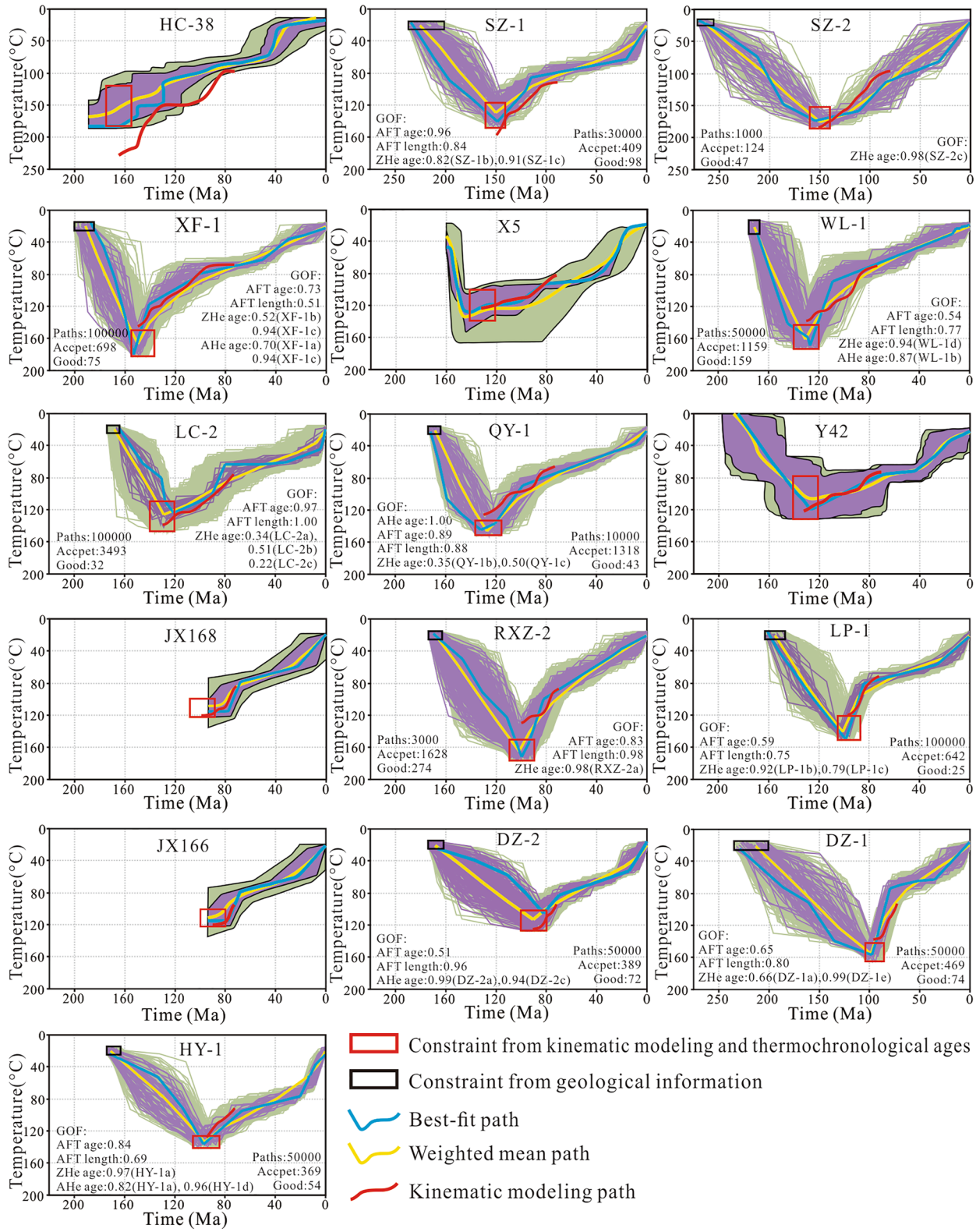

Figure 9. Modeled thermal histories of samples based on apatite fission track, AHe, and ZHe data and the *T-t* paths converted from the recorded kinematic uplift trajectories of samples. The good-fit and acceptable solutions are within the purple and green envelops/paths, respectively. The positions of the samples and corresponding particles are shown in Figures 1 and 5i, respectively. The solid red lines indicate the same temperature path as the sample tracks in Figure 6.

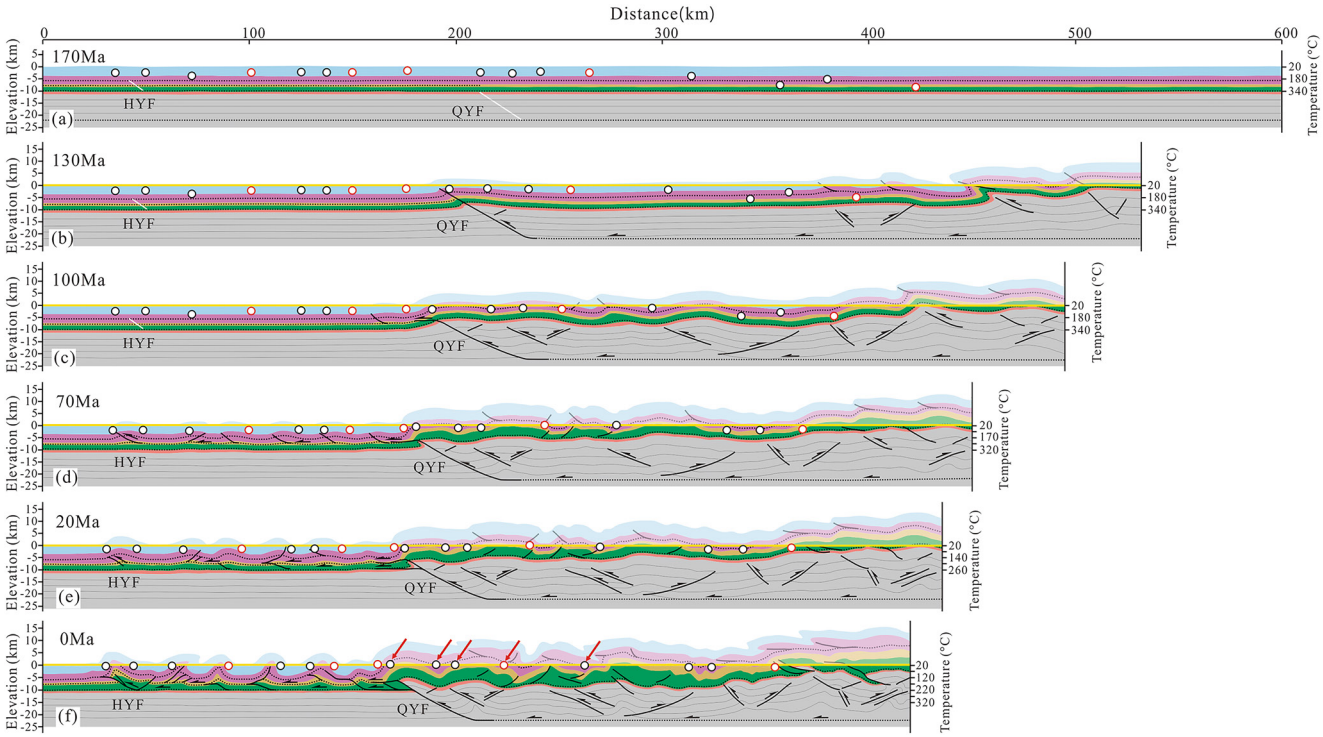

Figure 10. Balanced geological cross-section reconstructions in the Eastern Sichuan fold-and-thrust belt (see A-A' on Figure 1c for location). The white lines indicate the initial locations of Huayingshan fault and Qiyueshan fault. The red arrow marks samples showing different strata from the actual, because only the projected position of the sample is displayed on the balanced section. The yellow and dotted bold black lines indicate the surface and the décollement layer, respectively. The eroded part is filled with light color.

the present. The thermal history of sample RXZ-2 was characterized by a rapid cooling rate of 2.67°C/Ma from 100 Ma to 70 Ma and then a slow cooling rate of 0.86°C/Ma from 70 Ma until the present. The cooling process of sample LP-1 was characterized by a rapid cooling rate of 4.67°C/Ma during 100–85 Ma, a slow cooling rate of 0.33°C/Ma from 85 to 25 Ma, and a final rapid cooling rate of 1.60°C/Ma. Sample DZ-2 cooled from 113 to 86°C at a rate of ∼1.50°C/Ma during 88–70 Ma, experienced slow cooling at a rate of 0.62°C/Ma from 70 to 15 Ma, and finally underwent accelerated cooling at a rate of 2.13°C/Ma. Sample DZ-1 underwent rapid cooling at a rate of 6.88°C/Ma from 95 to 80 Ma, followed by slow cooling at a rate of 0.22°C/Ma during 80–35 Ma and an accelerated cooling at rate of 1.14°C/Ma after 35 Ma. Sample HY-1 cooled rapidly during 98–66 Ma. Its temperature decreased from 135 to 95°C, with a cooling rate of 2.19°C/Ma. Then, it underwent slow cooling during 66–20 Ma at a cooling rate of ∼0.43°C/Ma, followed by final accelerated cooling at a rate of 2.75°C/Ma.

4.4. Kinematic Restoration of the ESFTB

Based on the thermo-kinematic analysis, and results of analog models and discrete element numerical modeling, we restored geological cross-section A-A' using the 2DMOVE software. Ultimately, our results indicate that 27.6% shortening occurred within the thick-skinned domain and 22.1% of shortening in the thin-skinned domain. The results highlight the five major deformation stages of the ESFTB during the Mesozoic-Cenozoic. (a) Shortening above the basal decollement and formation of large imbricates separated by narrow synclines (during 170–130 Ma). During this stage, two large box anticlines formed between the QYF and the ZHY due to northwestward compression. The upper crustal structures were controlled by the deep basal décollement horizon. Then, the pre-existing QYF became active, inducing fault-propagation folding (Figure 10b). (b) The transition stage (during 130–100 Ma), which is characterized by a change from fault-propagation folding to fault-bend folding in the transition zone. QYF connects the deeper basal décollement horizon and the shallower décollement layers (Middle-Lower Cambrian, Silurian, and Middle-Lower Triassic), transferring deformation to the shallow layers. The hanging wall is continuously uplifted forming a thrust nappe. Simultaneously, several small decollement folds and fault-propagation folds developed in the shallow structural layer of the narrow synclines

(Figure 10c). (c) Stepping up of deformation to shallow decollement levels and shaping of the thick-skinned domain (during 100–70 Ma). At this stage, the shallow Silurian and Middle-Lower Triassic décollement layers controlled the deformation in the shallow layers northwest of QYF. Several narrow anticlines formed in the northwest. In addition, the narrow synclines were closed and complex anticlinoriums and synclinoriums were shaped (Figure 10d). (d) Shaping of the thin-skinned domain (during 70–20 Ma). During this stage, tightening of the anticlines and synclines was accompanied by enhanced displacement along the shallow thrusts and a Jura-type fold-and-thrust belt formed (Figure 10e). (e) The continuous exhumation and structural modification stage (from 20 Ma to present time). In the Late Eocene, the ESFTB experienced westward compression from the Tibetan Plateau and northwestward compression from the Jiangnan-Xuefengshan orogen. The thin-skinned domain was eroded rapidly, and the thick-skinned domain underwent continuous slow erosion (Figure 10f).

5. Discussion

5.1. Formation Mechanism of the ESFTB

Presence of multiple décollement layers and pre-existing faults have played a key role in the formation of the ESFTB, similar to the Zagros fold-and-thrust belt in Iran, which contains two major basement faults (the Mountain Front Fault and the Surmeh Fault) (Koyi and Cotton, 2004; Koyi & Mansurbeg, 2020; Yamato et al., 2011). Intermediate incompetent layers (shale, gypsum, marl, and mudstone) can act as weak horizons and drastically increase the growth rate of the folding instability, resulting in regularly spaced folds (Fernandez & Kaus, 2014; Koyi & Sans, 2006; Koyi & Cotton, 2004; Yamato et al., 2011). Results of analog models presented here support the hypothesis that the thick-skinned domain was mainly controlled by the basal décollement horizon, which is consistent with the conclusions of previous studies (C. X. Li et al., 2021; Yan et al., 2009). The thickness of the overlying strata or the depth of the décollement layer determines the wavelength of the décollement fold (Koyi & Mansourbeg, 2020; Massoli et al., 2006; Mitra, 2003). Based on interpretation of seismic section, C. X. Li et al. (2015) concluded that the wavelengths of the folds in the thin-skinned domain are approximately 10–20 km. Furthermore, the modeling results in the case where the Silurian strata is main controlling décollement layer are consistent with the wavelengths of 10–20 km (X. Q. Zhang et al., 2015). As such, we suggest that the thin-skinned domain is most likely detached above the shallower Silurian shale rather than the deeper Middle-Lower Cambrian shale and gypsum proposed by C. X. Li et al. (2021). Our modeling results also indicate that several fault-propagation folds along the Silurian décollement form an imbricate fan in the thin-skinned domain, whereas little slip and folding occurred in the Upper Cambrian-Ordovician strata (Figures 5e–5j).

The pre-existing QYF played a key role in the development of the Jura-type folds in the northwestern ESFTB. As shown in the models, this pre-existing fault had a significant effect on the evolution of the structures by transferring deformation between the deep and shallow detachment layers, as it has also been shown by Koyi and Mansourbeg (2020) in the Zagros FTB. Similar to the model results, it is assumed here that through fault-bend folding, the pre-existing fault connected the deep basal décollement horizon and the shallow décollement layers (Figure 5i). The hanging wall of the model QYF forms a broad anticline with flexural slip which eventually develops to a transition zone where displacement ramps up from deeper levels to shallower levels (Figures 5e and 5i). The pre-existing fault HYF also affected the evolution of the thin-skinned domain. Modeling results suggest that the Huayingshan anticline (samples HY-1 and DZ-1) was uplifted earlier than the Pubaoshan anticline (sample DZ-2) (Figures 1c, 6, and 9). Based on these results, we conclude that the ESFTB was formed by fault-related folding of the sedimentary cover above a flat-ramp trajectory composed of a basal décollement horizon (Archean strata of the middle crust), the deep, pre-existing fault QYF, the intermediate Silurian décollement horizon, and the shallow pre-existing fault HYF during northwestward shortening. This is similar to the proposed fault-bend fold model (C. M. Feng et al., 2008; Yan et al., 2003) and the fault-propagation and buckle fold model (Ding et al., 2007) suggested for the formation of the belt by previous researchers.

Geological cross-section A-A' (Figure 1c) and the analog modeling results (Figure 5) reveal that the basal décollement appears subhorizontal and the surface topography exhibits a gentle slope, suggesting that the ESFTB is characterized by a low-angle taper. Such low-angle taper is also reproduced in the analog modeling results (Figure 5). We propose that a high lateral/basal shear stress (τ_s/τ_d) ratio ($\tau_s/\tau_d = 5.5$, in the analog models of this study) due to the presence of a weak basal décollement is probably the key factor responsible for the gentle taper of the ESFTB. Natural fold-and-thrust belts are generally characterized by a weak basal layer (Chapple, 1978). Thickness, strength, and rheology (frictional or viscous) of the weak base influence the deformation style of the

overlying layers (David & Engelder, 1985; Dahlen, 1988, 1990). Several studies using analog and numerical models confirm that a decrease in basal strength decreases the critical taper (Burbidge & Braun, 2002; Cotton & Koyi, 2000; Koyi & Vendeville, 2003; Mulugeta, 1988; Naylor et al., 2005; Nilforoushan et al., 2008; Teixell & Koyi, 2003). Results of several of these modeling studies can be shown to fit the predictions of critical taper theory (Davis et al., 1983; Dahlen, 1990). A weak basal decollement leads to a wedge built through frontal accretion with a shallow taper angle and a more symmetric deformation style (Buiter, 2012; David & Engelder, 1985). Analog modeling revealed that an increase in the value of τ_s/τ_d ratio in thrust wedges leads to a decrease in taper angle (Zhou and Zhou, 2022).

5.2. Tectonic Implications of Cooling Histories

The thermal regime or thermal background is of significant importance in analyzing geodynamic processes in the continental lithosphere (Furlong & Chapman, 1987; Lachenbruch & Sass, 1977; Pollack & Chapman, 1977; Qiu et al., 2022; Reiners & Brandon, 2006). Cooling from peak levels is typically interpreted as the result of uplift and regional exhumation in response to tectonic events or denudation (Chang et al., 2021). It is generally believed that recorded cooling events are the result of denudation (Deng et al., 2013; C. X. Li et al., 2021; Richardson et al., 2008; H. C. Shi et al., 2016; Tian et al., 2018). All of the modeling results (Figure 9) reveal the occurrence of periodic cooling after the maximum temperatures were reached. In general, the thermo-kinematic models indicate that the samples experienced thermal histories comprised of two or three distinct stages. Samples HY-1 and DZ-2 from the thin-skinned domain (Figure 1c) experienced rapid-slow-rapid cooling processes, while sample QY-1 from the transition zone (Figure 1c) and samples WL-1 and XF-1 from the thick-skinned domain (Figure 1c) underwent a rapid-slow two-stage cooling process. The thermal histories of these five samples are characterized by a first phase of rapid cooling during 150 to 88 Ma, followed by a period of slow cooling with the temperature decreased slowly from ~90 to ~50°C from the Late Cretaceous to the Miocene. The onset of final accelerated cooling to surface temperatures occurred in the thin-skinned domain between 20 and 15 Ma.

During the Late Jurassic, South China evolved into an Andean-type active margin due to the approximately northwestward subduction of the Paleo-Pacific Plate (C. H. Xu et al., 2017). The synchronous convergence generated distant effects, including intracontinental deformation and associated magmatism, during the Yanshanian orogeny (Y. Q. Zhang et al., 2021). The continued northwestward subduction of the Paleo-Pacific Plate resulted in northwestward shortening across South China in the Late Jurassic. It is generally believed that the progressive deformation of the ESFTB was controlled by this northwestward convergence (C. X. Li et al., 2021; S. F. Liu et al., 2005; Lu et al., 2020; W. Shi et al., 2015). Our thermochronological data constrain the timing of the rapid exhumation in the ESFTB to 150–88 Ma, which also supports crustal shortening in South China to be associated with the subduction of the Paleo-Pacific Plate.

Chu et al. (2019) and J. H. Li et al. (2020) proposed a model for the Late Jurassic-Cretaceous tectonic evolution of South China, where they suggested an ongoing slab subduction and retreat to cause the slab to undergo eclogitization and to ultimately break-off. Subsequent low-angle subduction, which may have been due to slab rebound, resulted in crustal shortening and a magmatic lull in the late Early Cretaceous. Continuous slab subduction may have again led to slab steepening, re-initiation of crustal extension, and magmatism during the Late Cretaceous. Previous studies suggested that the rate of convergence of the Pacific and Eurasian plates decreased from ~120 to 140 mm/yr in the Late Cretaceous to ~30–40 mm/yr in the Eocene, and then, it increased to ~70–110 mm/yr from the Oligocene to the Early Miocene (J. H. Li et al., 2014; Northrup et al., 1995). These changes in the convergence rate of the Pacific and Eurasia plates may have caused the rollback of the subducted Pacific slab and the formation of a NW-SE-trending extensional stress field in South China (Ren et al., 2002). During the Cretaceous, South China was characterized by widespread extensional tectonics and formation of basins (e.g., the Yuanma Basin in the Jiangnan-Xuefengshan orogen and coastal volcanic basins) (J. H. Li et al., 2012, 2014) and lava domes formed through rapid exhumation in the Late Cretaceous (e.g., the 136–80 Ma Hengshan, 132–95 Ma Lianyunshan-Mufushan, 126 Ma Lushan, and 100–85 Ma Yuechengling domes in the Jiangnan-Xuefengshan orogen) (Chu et al., 2019; Ji et al., 2018; J. H. Li et al., 2016; Lin et al., 2000). Across South China, the NW-SE crustal extension generated numerous NE-striking normal faults (J. H. Li et al., 2014; Sternai et al., 2014; E. Wang et al., 2014; Yuan et al., 2010). A field investigation of fault-slip data collected from different rock units and the documented polyphase tectonic stress fields in the Yuanma Basin suggest that the extensional phase seems to have lasted through the Early Paleogene and ended in the Late Paleogene when it changed to a compressional

regime with NE-SW compression and NW-SE extension (J. H. Li et al., 2012). A key feature of all of the thermal history models of South China is the requirement of rapid cooling in the Latest Cretaceous followed by a period of relatively stable temperature, which is consistent with the cessation of significant exhumation. Examples of the thermal history models of South China showing rapid cooling in the Latest Cretaceous followed by a period of relatively stable temperature include the Jiangnan-Xuefengshan orogen (J. H. Li et al., 2016), the ESFTB (Richardson et al., 2008; H. C. Shi et al., 2016; this study, Figure 9), and the Longmenshan Micangshan and the Dabashan in the Sichuan Basin (Deng et al., 2013; Tian et al., 2012a, 2012b, 2013). The timing of the changes in the extensional stress field are consistent with the changes in the exhumation rate in proposed thermal history models. Thus, we infer that the decrease in the exhumation rate during the Late Cretaceous-Miocene was related to the crustal extension in South China.

The thermal histories constrained by the AFT, AHe, and ZHe ages show that the thin-skinned domain experienced a rapid cooling since the Miocene, while the transition zone and the thick-skinned domain underwent a long, slow cooling since the Late Cretaceous. The different Cenozoic cooling processes in the different domains may have different tectonic implications. The Cenozoic Indian plate subduction and later collision with Eurasian plate resulted in the uplift of the Qinghai-Tibet Plateau and lateral shearing along the Xianshuihe fault in the Yangtze Block (Sternai et al., 2014; Tong et al., 2019; E. Wang et al., 2014). There is growing thermochronological evidence of the occurrence of rapid erosion across the Sichuan Basin during the Cenozoic (e.g., at 10–20 Ma in the Longmenshan fault belt, at 16 Ma in the Micangshan, at 30–40 Ma in the central paleo-uplift in the Sichuan Basin, and at 15–40 Ma in the eastern Sichuan Basin) (Deng et al., 2018; W. Liu et al., 2018; Richardson et al., 2008; Tian et al., 2012a, 2018; Yang et al., 2017). Our new results indicate that the final stage of accelerated exhumation in the thin-skinned domain began at 15–20 Ma. The onset of rapid cooling has a trend of eastward and northeastward propagation in the Sichuan Basin (H. C. Shi et al., 2016). The Late Eocene-Miocene phase of accelerated exhumation occurred synchronously with the early phase of eastward growth and extrusion of the Tibetan Plateau (E. Wang et al., 2012). In addition, surface geological mapping and seismic surveys of the northern part of the thin-skinned domain suggest that the fault is west dipping, indicating an eastward growth of the Tibetan Plateau resulting in the shallow crustal shortening of the Sichuan basin (Tian et al., 2018). Seismic reflection studies also indicate that the major tectonostratigraphic layers (Mesozoic-Paleozoic strata) are mostly west dipping across the Sichuan Basin (Gao et al., 2016). The E-W shortening in the thin-skinned domain can be explained by west dipping reverse faulting originating from a basin-scale detachment (Tian et al., 2018). The Miocene shortening in the thin-skinned domain is consistent with the stepwise growth of the evolution of the Tibetan Plateau (Hubbard & Shaw, 2009; Replumaz & Tapponnier, 2003; Tapponnier et al., 2001). Based on the structural and thermochronological evidence, we conclude that the accelerated cooling in the thin-skinned domain since the Miocene was a response to the far-field effects of the eastward growth of the Tibetan Plateau.

Whether or not the eastward growth of the Tibetan Plateau affected the tectonic evolution of the thick-skinned domain and the eastern Yangtze Block remains controversial. Deformation in Qinling to the north and the Yangtze Block to the east is incompatible with shallow crustal shortening in the Sichuan Basin (Tian et al., 2018). The Cenozoic deformation in Qinling was mainly transtensional (Z. N. Liu et al., 2013; E. Wang et al., 2003) and that in the Yangtze Block (southeast of the QYF) was extensional (S. F. Liu et al., 2003; Yuan et al., 2010). This suggests that the Cenozoic transtensional and extensional deformation in Qinling and the Yangtze Block (southeast of the QYF) may not have resulted from the eastward growth of the Tibetan Plateau. Analog modeling investigations of hanging wall accommodation above a flat-ramp-flat footwall have revealed that deformation in the hanging wall was dominated by layer-parallel thickening and the generation of a series of back thrusts (Bonini et al., 2000; Koyi & Sans, 2006; Rosas et al., 2017). We also conducted another analog model, and it was observed that the shortening direction was consistent with the dip of the pre-existing fault. The experiment parameters are same to these in the Table 1. The analog modeling results revealed that deformation all occurred in front of the moving back wall and no structures formed in the hanging wall (Figure 11). The pre-existing faults inhibited thrusts forward-propagating. The Cenozoic shallow crustal shortening resulting from the eastward growth of the Tibetan Plateau was consistent with the dip of the pre-existing QYF in the ESFTB. Modeling results indicate that the pre-existing model equivalent of QYF may have inhibited eastward crustal shortening from causing deformation in the model equivalent of thick-skinned domain. Therefore, we postulate that the eastward growth of the Tibetan Plateau had little effect on the Cenozoic deformation in the thick-skinned domain.

Little AHe data have been reported in the thick-skinned domain. This study is the first AHe geochronological evidence reported for dating the Cenozoic phase of shortening in the thick-skinned domain. The difference

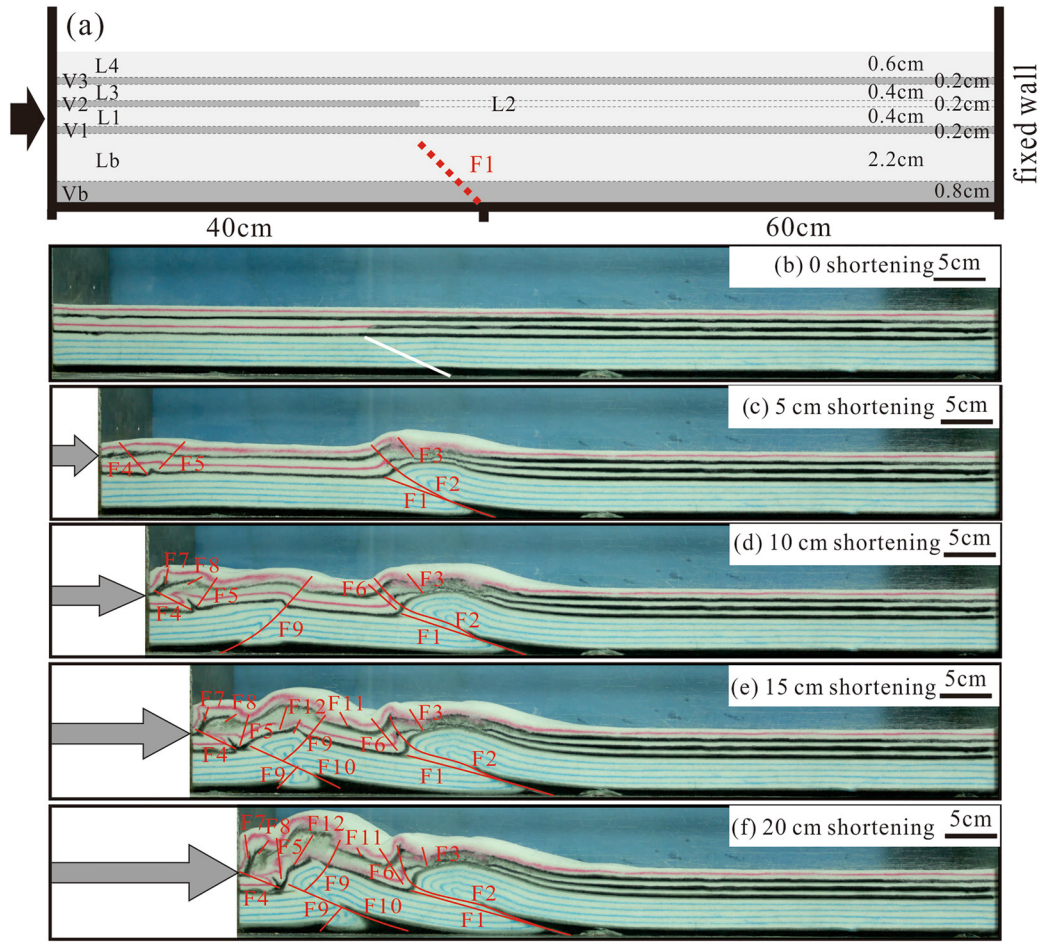

Figure 11. (a) Initial model setup of the analog model. F1 represents a pre-existing fault. (b–f) Sequential sidewall views of model. *F* represent thrust faults which are numbered in the order of their formation.

in the Cenozoic cooling processes between the thick-skinned domain and the thin-skinned domain suggests different tectonic responses. Inversion structures involving the Lower Tertiary strata have been observed on seismic profiles in the Mesozoic-Cenozoic basins in the thick-skinned domain and Middle-Lower Yangtze Block (southeast of the QYF) (S. F. Liu et al., 2003; Shinn et al., 2010). A systematic study, involving tectonics, sedimentation, AFT, and dynamic topography, revealed that inversion of these basins is related to the subduction retreat of the Paleo-Pacific Plate (Suo et al., 2020). The thermal structure of the East Asian continental lithosphere shows that the Cathaysia Block in the southeastern part of South China has a hot mantle lithosphere and high temperature anomalies. High heat flow from the upper mantle is the main cause of the high surface heat flow and the relatively thin lithosphere. The hot asthenosphere is attributed to the subduction of the Pacific Plate. This suggests that the subduction of the Paleo-Pacific Plate still has a significant impact on the East Asian continent at present (Sun et al., 2022). The seismic tomography shows that there are low velocity anomalies in the upper mantle, which also suggests the effect of the subduction of the Paleo-Pacific Plate on the East Asian continent (Guo et al., 2018; He, 2019; Zhao et al., 2017). The correlation between the distribution of the volcanoes and the depth isolines of the Benioff zone of the Pacific Plate and the front of the stagnant slab (X. Liu et al., 2017; Zhao, 2021) further indicate that the asthenospheric disturbance caused by the subducted and stagnated Pacific Plate may have affected the Mongolian Plateau and Lake Baikal (W. L. Xu et al., 2020). In summary, the subducted and stagnated Pacific Plate caused a wide range of tectonic responses in East Asia, which inevitably has an impact on the geomorphic evolution of the ESFTB. Therefore, we infer that the Cenozoic extension and continuous slow cooling in the thick-skinned domain was most likely associated with the continuous crustal extension in South China, which resulted from the slab retreat of the Paleo-Pacific Plate.

5.3. Prospects of Thermo-Kinematic Analysis

Kinematic restoration is applied to fold-and-thrust belts using field data and seismic-profiles, as well as through dynamic characterization using analog modeling, balanced reconstruction, and thermochronology (Bonnet et al., 2007; Boyer & Elliot, 1982; Dominguez et al., 2000; Dong et al., 2020; Horton, 2018; Kyle, 1996; Kohn & Gleadow, 2018; Teixell & Koyi, 2003; Tian et al., 2016). The goal of kinematic restoration of balanced cross sections is to obtain a reliable cross section of the changing geometry of structures over time. Modeling, involving analog models, finite element and DEMs, and forward simulation of fold-and-thrust belts, are convenient in terms of portraying the geometric, kinematic and in many cases the dynamic evolution of fold-and-thrust belts. However, when certain parameters from the natural prototype are missing, the simulations may become incomplete. For example, in areas where the strata have been eroded, kinematic restorations become complicated and subjective due to imprecise assessment of timing, rate, and extent of deformation and erosion. Thermochronology can be used to simulate the tectonic evolution by reconstructing the thermal histories of samples from the major structures within a belt. Such an approach is better for quantitatively characterizing the magnitude and timing of deformation. However, some time-temperature constraints are required to reconstruct the thermal histories. Different hypotheses regarding the tectonic background and dynamic mechanism will inevitably lead to different constraints and different thermal histories. In addition, the thermal history obtained using the HeFTy or QTQt software, which revealed the cooling processes of the samples, did not consider the impact of flexural slip information, which has a significant effect on the structural analysis of a region with a long lateral slip distance.

Several studies have focused on restoration of the kinematic evolution of intracontinental fold-and-thrust belts using thermo-kinematic models (Almendral et al., 2015; Buford & McQuarrie, 2019; Chapman et al., 2017; Mora et al., 2015). For example, lateral variations in the deformation and exhumation rates in the Central Andes were quantified based on integration of the geology, ages, and locations of reset thermochronometer systems and the synorogenic sediment distribution (Buford & McQuarrie, 2019). Thrusting and exhumation histories of the Colombian Eastern Cordillera (Almendral et al., 2015; Mora et al., 2015) and Tajik fold-and-thrust belt (Chapman et al., 2017) were constrained using the FetKin approach and coupling of the balanced reconstruction and the finite element computation of the temperature and thermochronological data.

Through applying a thermo-kinematic approach, we have attempted to reconstruct the tectonic and thermal evolution of a complex orogen (i.e., ESFTB) and establish a visual link between the regional kinematic processes and the thermochronology of the local structures. The kinematic simulation provided more reasonable and comprehensive geological constraints for the thermochronologcal investigation. Based on this, we used an analog model, a discrete element numerical simulation, AFT and ZHe ages, and a reconstructed balanced profile as the thermo-kinematic constraints on the Mesozoic-Cenozoic tectonic uplift of the ESFTB. The technical breakthrough of this study is to apply thermo-kinematic approach to establish an accurate geological model in an area with multiple decollement horizons. It should be noted that the thermo-kinematic approach which we used in this study also has some limitations. For example, the temperature path converted from the recorded kinematic path of the particles may not match the thermal histories well. We have compared the thermal histories with the *T-t* path converted from the recorded kinematic uplift trajectories of the samples. Except for samples HY-1, LC-2, JX166, and Y42, the *T-t* paths of other samples are not in good agreement with the particle trajectories (model equivalent to samples DZ-1, DZ-2, LP-1, RXZ-2, JX168, QY-1, WL-1, XF-1, SZ-2, SZ-1, X5, and HC-38) (Figure 9). There may be two reasons for this discrepancy. First, analog models and the DEM cannot be used to perfectly restore the amplitude of the structural uplift. In contrast to the analog model, in the numerical model, a larger vertical displacement occurred in the hanging wall of the model QYF, and a smaller vertical displacement developed in the model-equivalent Jiangnan-Xuefengshan orogen and the thin-skinned domain. Only three fault-propagation folds formed in the thin-skinned domain even when the model was run for a long time. In addition, the shallow décollement layers deformed less than their equivalents in the hinterland. Second, the geothermal gradient plays an important role in the transformation of the kinematic path into the temperature path. An inaccurate geothermal gradient may result in a great difference between temperature path converted from the recorded kinematic path of the particle and natural thermal history. It is necessary to reconstruct the paleo-geothermal gradient using a series of vitrinite reflectance data and to further improve the accuracy and rationality of the thermo-kinematic analysis. Analog models and the DEM can be used to accomplish the kinematic restoration of fold-and-thrust belts and the onset of the deformation of the major thrust sheets can be determined relatively well. Combining the approach used, that is, a combination of analog- and numerical modeling, geological section balancing, and their integration with regional geology and thermochronology, provide a holistic approach which may become

"standard" in future. It is worthwhile to underline that the thermo-kinematic approach can be further developed to include and combine the kinematic forward (analog model), kinematic inversion (balanced cross-section), and thermochronology forward and inversion methods.

6. Conclusions

In this study, a new thermo-kinematic approach that combines analog modeling, DEM simulation, balanced reconstruction, and thermochronological data are used to constrain kinematic evolution of the ESFTB. A thermo-kinematic workflow is presented for reconstructing the tectono-thermal evolution of the belt, and establish a geometric link between the regional kinematics and the thermochronology of the local structures. Restoration shows that the ESFTB experienced northwestward thrusting during the Mesozoic-Cenozoic and its evolution can be subdivided into five major stages: shortening above the basal decollement and formation of large imbricates separated by narrow synclines (during 170–130 Ma), a transition stage (during 130–100 Ma), stepping up of deformation to shallow decollement levels and shaping of the thick-skinned domain (during 100–70 Ma), shaping of the thin-skinned domain (during 70–20 Ma), and a continuous exhumation and structural modification stage (from 20 Ma to present).

Fault-related folding in the sedimentary cover above a flat-ramp staircase was dominating during northwestward shortening of the ESFTB, which includes a basal décollement horizon (Archean strata of the middle crust), a deep pre-existing fault (QYF), an intermediate Silurian décollement horizon, and a shallow pre-existing fault (HYF). Shortening in the ESFTB with such combination of elements resulted in the formation of forward breaking thrusting. The pre-existing QYF connected the deeper basal décollement horizon with the shallower Silurian décollement layer and had a significant effect on the evolution of ESFTB as it has been also reproduced in the models presented in this study.

The ESFTB experienced periodic exhumation throughout the Mesozoic-Cenozoic. The thick-skinned domain and transition zone experienced two stages of exhumation characterized by rapid exhumation during the Early-Late Cretaceous followed by slow exhumation from the Late Cretaceous to the present. The thin-skinned domain experienced an initial rapid exhumation during the Early-Late Cretaceous, followed by a slow exhumation until the Miocene, which was in turn followed by accelerated exhumation since then. Changes in the exhumation rates were in response to the Mesozoic subduction retreat of the Paleo-Pacific Plate and the Cenozoic eastward growth of the Tibetan Plateau. The westward subduction of the Paleo-Pacific Plate resulted in rapid exhumation from the Late Jurassic to the Late Cretaceous. The crustal extension associated with the rollback of the Paleo-Pacific slab caused a decrease in the Mesozoic exhumation rate. An accelerated cooling in the thin-skinned domain in the Miocene was a response to the far-field effects of the eastward growth of the Tibetan Plateau, while the Cenozoic continuous slow exhumation in the thick-skinned domain was related to the continuous crustal extension in South China.

Data Availability Statement

We confirm that the data supporting the findings of this study are available within Supporting Information S1. The low-temperature thermochronology data will eventually be deposited in the Mendeley Data (https://data.mendeley.com/datasets/4kzmgj5jd2/1).

Acknowledgments
The National Natural Science Foundation of China (No. 41830424, U2244208, 42302138, U19B6003, 42002173) and China Postdoctoral Science Foundation (No. 2023M733869) provided financial support. Jixin Zhang and Shuaiyu Shi gave technical support to physical simulation. Prof. Zhina Liu gave helpful suggestions and provided the PFC2D software.

References

Allmendinger, R. W. (1998). Inverse and forward numerical modeling of trishear fault-propagation folds. *Tectonics*, *17*(4), 640–656. https://doi.org/10.1029/98TC01907

Almendral, A., Robles, W., Parra, M., Mora, A., Ketcham, R., & Raghib, M. (2015). FetKin: Coupling kinematic restorations and temperature to predict thrusting, exhumation histories, and thermochronometric ages. *AAPG Bulletin*, *99*(08), 1557–1573. https://doi.org/10.1306/07071411112

Bonini, M. (2003). Detachment folding, fold amplification, and diapirism in thrust wedge experiments. *Tectonics*, *22*(6), 1065. https://doi.org/10.1029/2002TC001458

Bonini, M. (2007). Deformation patterns and structural vergence in brittle-ductile thrust wedges: An additional analogue modelling perspective. *Journal of Structural Geology*, *29*(1), 141–158. https://doi.org/10.1016/j.jsg.2006.06.012

Bonini, M., Sani, F., & Antonielli, B. (2012). Basin inversion and contractional reactivation of inherited normal faults: A review based on previous and new experimental models. *Tectonophysics*, *522–523*, 55–88. https://doi.org/10.1016/j.tecto.2011.11.014

Bonini, M., Sokoutis, D., Mulugeta, G., & Katrivanos, E. (2000). Modelling hanging wall accommodation above rigid thrust ramps. *Journal of Structural Geology*, *22*(8), 1165–1179. https://doi.org/10.1016/S0191–8141(00)00033-X

Bonnet, C., Malavieille, J., & Mosar, J. (2007). Interactions between tectonics, erosion, and sedimentation during the recent evolution of the Alpine orogen: Analogue modeling insights. *Tectonics*, *26*(6), TC6016. https://doi.org/10.1029/2006TC002048
Boyer, S. E., & Elliot, D. (1982). Thrust system. *AAPG Bulletin*, *66*, 1196–1230. https://doi.org/10.1306/03B5A77D-16D1-11D7-8645000102C1865D
Buford, P. V. M., & McQuarrie, N. (2019). Kinematic, flexural, and thermal modelling in the Central Andes: Unravelling age and signal of deformation, exhumation, and uplift. *Tectonophysics*, *766*, 302–325. https://doi.org/10.1016/j.tecto.2019.06.008
Buiter, S. J. (2012). A review of brittle compressional wedge models. *Tectonophysics*, *530*, 1–17. https://doi.org/10.1016/j.tecto.2011.12.018
Burbidge, D. R., & Braun, J. (2002). Numerical models of the evolution of accretionary wedges and fold-and-thrust belts using the distinct-element method. *Geophysical Journal International*, *148*(3), 542–561. https://doi.org/10.1046/j.1365-246x.2002.01579.x
Carlson, W. D., Donelick, R. A., & Ketcham, R. A. (1999). Variability of apatite fission-track annealing kinetics: I. Experimental results. *American Mineralogist*, *84*(9), 1213–1223. https://doi.org/10.2138/am-1999-0901
Chang, J., Glorie, S., Qiu, N. S., Min, K., Xiao, Y., & Xu, W. (2021). Late Miocene (10.0~6.0 Ma) rapid exhumation of the Chinese South Tianshan: Implications for the timing of aridification in the Tarim Basin. *Geophysical Research Letters*, *48*(3), e2020GL090623. https://doi.org/10.1029/2020GL090623
Chang, J., Li, D., Min, K., Qiu, N. S., Xiao, Y., Wu, H., & Liu, N. (2019a). Cenozoic deformation of the Kalpin fold-and-thrust belt, southern Chinese Tian Shan: New insights from low-T thermochronology and sandbox modeling. *Tectonophysics*, *766*, 416–432. https://doi.org/10.1016/j.tecto.2019.06.018
Chang, J., Qiu, N. S., Liu, S., Cai, C. E., Xu, Q. C., & Liu, N. (2019b). Post-Triassic multiple exhumation of the Taihang Mountains revealed via low-T thermochronology: Implications for the paleo-geomorphologic reconstruction of the North China Craton. *Gondwana Research*, *68*, 34–49. https://doi.org/10.1016/j.gr.2018.11.007
Chapman, J. B., Carrapa, B., Ballato, P., DeCelles, P. G., Worthington, J., Oimahmadov, I., et al. (2017). Intracontinental subduction beneath the Pamir Mountains; constraints from thermokinematic modeling of shortening in the Tajik fold-and-thrust belt. *Geological Society of America Bulletin*, *129*(11–12), 1450–1471. https://doi.org/10.1130/B31730.1
Chapple, W. M. (1978). Mechanics of thin-skinned fold-and-thrust belts. *Geological Society of America Bulletin*, *89*(8), 1189–1198. https://doi.org/10.1130/0016-7606(1978)89<1189:MOTFB>2.0.CO;2
Cheng, Y. M., Liu, Z. N., Song, W. D., & Au, S. K. (2009). Laboratory test and particle flow simulation of silos problem with nonhomogeneous materials. *Journal of Geotechnical and Geoenvironmental Engineering*, *135*(11), 1754–1761. https://doi.org/10.1061/(ASCE)GT.1943-5606.0000125
Chu, Y., Faure, M., Lin, W., & Wang, Q. C. (2012). Early Mesozoic tectonics of the South China block: Insights from the Xuefengshan intracontinental orogen. *Journal of Asian Earth Sciences*, *61*, 199–220. https://doi.org/10.1016/j.jseaes.2012.09.029
Chu, Y., Lin, W., Faure, M., Wang, Q. C., & Ji, W. (2012). Phanerozoic tectonothermal events of the Xuefengshan Belt, central South China: Implications from U–Pb age and Lu–Hf determinations of granites. *Lithos*, *150*, 243–255. https://doi.org/10.1016/j.lithos.2012.04.005
Chu, Y., Lin, W., Faure, M., Xue, Z. H., Ji, W. B., & Feng, Z. T. (2019). Cretaceous episodic extension in the South China block, East Asia: Evidence from the Yuechengling massif of central South China. *Tectonics*, *38*(10), 3675–3702. https://doi.org/10.1029/2019TC005516
Cogné, N., Chew, D. M., Donelick, R. A., & Ansberque, C. (2020). LA-ICP-MS apatite fission track dating: A practical zeta-based approach. *Chemical Geology*, *531*, 119302. https://doi.org/10.1016/j.chemgeo.2019.119302
Costa, E., & Vendeville, B. (2002). Experimental insights on the geometry and kinematics of fold-and-thrust belts above weak, viscous evaporitic décollement. *Journal of Structural Geology*, *24*, 1729–1739. https://doi.org/10.1016/s0191-8141(01)00169-9
Cotton, J. T., & Koyi, H. A. (2000). Modeling of thrust fronts above ductile and frictional detachments: Application to structures in the Salt Range and Potwar Plateau, Pakistan. *Geological Society of America Bulletin*, *112*(3), 351–363. https://doi.org/10.1130/0016-7606(2000)112<351:MOTFAD>2.0.CO;2
Cundall, P. A., & Strack, O. D. (1979). A discrete numerical model for granular assemblies. *Geotechnique*, *29*(1), 47–65. https://doi.org/10.1680/geot.1979.29.1.47
Dahlen, F. A. (1988). Mechanical energy budget of a fold-and-thrust belt. *Nature*, *331*(6154), 335–337. https://doi.org/10.1038/331335a0
Dahlen, F. A. (1990). Critical taper model of fold-and-thrust belts and accretionary wedges. *Annual Review of Earth and Planetary Sciences*, *18*, 55–99. https://doi.org/10.1146/annurev.ea.18.050190.000415
Davis, D. M., & Engelder, T. (1985). The role of salt in fold-andthrust belts. *Tectonophysics*, *119*(1-4), 67–88. https://doi.org/10.1016/0040-1951(85)90033-2
Davis, D., Suppe, J., & Dahlen, F. A. (1983). Mechanics of fold-and-thrust belts and accretionary wedges. *Journal of Geophysical Research*, *88*(B2), 1153–1172. https://doi.org/10.1029/JB088iB02p01153
Deng, B., Liu, S. G., Jiang, L., Zhao, G. P., Huang, R., Li, Z. W., et al. (2018). Tectonic uplift of the Xichang Basin (SE Tibetan Plateau) revealed by structural geology and thermochronology data. *Basin Research*, *30*(1), 75–96. https://doi.org/10.1111/bre.12243
Deng, B., Liu, S. G., Li, Z., Jansa, L. F., Liu, S., Wang, G. Z., & Sun, W. (2013). Differential exhumation at eastern margin of the Tibetan Plateau, from apatite fission-track thermochronology. *Tectonophysics*, *591*, 98–115. https://doi.org/10.1016/j.tecto.2012.11.012
Ding, D. K., Guo, T. L., Hu, M. X., & Liu, Y. L. (2007). Basement decoupling structure in Jiannan-Xuefeng-Series 1 of the southern structure studies. *Petroleum Geology & Expeiment*, *29*(2), 120–132.
Dominguez, S., Malavieille, J., & Lallemand, S. E. (2000). Deformation of accretionary wedges in response to seamount subduction: Insights from sandbox experiments. *Tectonics*, *19*(1), 182–196. https://doi.org/10.1029/1999TC900055
Donelick, R. A., O'Sullivan, P. B., & Ketcham, R. A. (2005). Apatite fission-track analysis. *Reviews in Mineralogy and Geochemistry*, *58*(1), 49–94. https://doi.org/10.2138/rmg.2005.58.3
Dong, S. W., Li, J. H., Cawood, P. A., Gao, R., Zhang, Y. Q., & Xin, Y. J. (2020). Mantle influx compensates crustal thinning beneath the Cathaysia Block, South China: Evidence from SINOPROBE reflection profiling. *Earth and Planetary Science Letters*, *544*, 116360. https://doi.org/10.1016/j.epsl.2020.116360
Dong, S. W., Zhang, Y. Q., Gao, R., Su, J. B., Liu, M., & Li, J. H. (2015). A possible buried Paleoproterozoic collisional orogen beneath central South China: Evidence from seismic-reflection profiling. *Precambrian Research*, *264*, 1–10. https://doi.org/10.1016/j.precamres.2015.04.003
Dunkl, I. (2002). Trackkey: A windows program for calculation and graphical presentation of fission track data. *Computers & Geosciences*, *28*(1), 3–12. https://doi.org/10.1016/S0098-3004(01)00024-3
Egan, S. S., Kane, S., Buddin, T. S., Williams, G. D., & Hodgetts, D. (1999). Computer modelling and visualisation of the structural deformation caused by movement along geological faults. *Computers & Geosciences*, *25*(3), 283–297. https://doi.org/10.1016/S0098-3004(98)00125-3
Farley, K. A. (2002). (U-Th)/He dating: Techniques, calibrations, and applications. *Reviews in Mineralogy and Geochemistry*, *47*(1), 819–844. https://doi.org/10.2138/rmg.2002.47.18
Feng, C. M., Liu, J., & Song, L. J. (2008). Formation mechanism of the tectonic deformation belt and the prognosis of favorable oil and gas exploration areas in the Middle and Upper Yangtze valley. *Acta Geoscientia Sinica*, *2*, 199–204. https://doi.org/10.3321/j.issn:1006-3021.2008.02.010

Feng, Q. Q., Qiu, N. S., Fu, X. D., Li, W. Z., Xu, Q., Li, X., & Wang, J. (2021). Permian geothermal units in the Sichuan Basin: Implications for the thermal effect of the Emeishan mantle plume. *Marine and Petroleum Geology*, *132*, 105226. https://doi.org/10.1016/j.marpetgeo.2021.105226

Fernandez, N., & Kaus, B. J. P. (2014). Fold interaction and wavelength selection in 3D models of multilayer detachment folding. *Tectonophysics*, *632*, 199–217. https://doi.org/10.1016/j.tecto.2014.06.013

Fitzgerald, P. G., & Malusà, M. G. (2018). *Concept of the exhumed partial annealing (retention) zone and age-elevation profiles in thermochronology*. Springer International Publishing.

Flowers, R. M., Ketcham, R. A., Shuster, D. L., & Farley, K. A. (2009). Apatite (U-Th)/He thermochronometry using a radiation damage accumulation and annealing model. *Geochimica et Cosmochimica Acta*, *73*(8), 2347–2365. https://doi.org/10.1016/j.gca.2009.01.015

Flowers, R. M., Shuster, D. L., Wernicke, B. P., & Farley, K. A. (2007). Radiation damage control on apatite (U-Th)/He dates from the Grand Canyon region, Colorado Plateau. *Geology*, *35*(5), 447. https://doi.org/10.1130/G23471A.1

Fraser, K. I., Enkelmann, E., Jess, S., Gilbert, H., & Grieco, R. (2021). Resolving the Cenozoic history of rock exhumation along the central rocky mountain trench using apatite low-temperature thermochronology. *Tectonics*, *40*(10), 1–25. https://doi.org/10.1029/2021TC006847

Furlong, K., & Chapman, D. S. (1987). Thermal state of the lithosphere. *Reviews of Geophysics*, *25*(6), 1255–1264. https://doi.org/10.1029/RG025i006p01255

Galibraith, R. F., & Green, P. F. (1990). Estimating the component ages in a finite mixture. *Nuclear Tracks and Radiation Measurements*, *17*(3), 197–206. https://doi.org/10.1016/1359-0189(90)90035-V

Gao, R., Chen, C., Wang, H. Y., Lu, Z. W., Brown, L., Dong, S. W., et al. (2016). SINOPROBE deep reflection profile reveals a Neo-Proterozoic subduction zone beneath Sichuan Basin. *Earth and Planetary Science Letters*, *454*, 86–91. https://doi.org/10.1016/j.epsl.2016.08.030

Gleadow, A. J. W., Belton, D. X., Kohn, B. P., & Brown, R. W. (2002). Fission track dating of phosphate minerals and the thermochronology of apatite. *Reviews in Mineralogy and Geochemistry*, *48*(1), 579–630. https://doi.org/10.2138/rmg.2002.48.16

Gleadow, A. J. W., Duddy, I. R., Green, P. F., & Hegarty, K. A. (1986). Fission track lengths in the apatite annealing zone and the interpretation of mixed ages. *Earth and Planetary Science Letters*, *78*(2), 245–254. https://doi.org/10.1016/0012-821X(86)90065-8

Gleadow, A. J. W., Harrison, M., Kohn, B. P., Lugo-Zazueta, R., & Phillips, D. (2015). The fish Canyon Tuff: A new look at an old low-temperature thermochronology standard. *Earth and Planetary Science Letters*, *424*, 95–108. https://doi.org/10.1016/j.epsl.2015.05.003

Green, P. F., Duddy, I. R., Gleadow, A. J. W., Tingate, P. R., & Laslett, G. M. (1986). Thermal annealing of fission tracks in apatite: 1. A qualitative description. *Chemical Geology: Isotope Geoscience section*, *59*, 237–253. https://doi.org/10.1016/0168-9622(86)90074-6

Gu, Z. D., Wang, X., Nunns, A., Zhang, B., Jiang, H., Fu, L., & Zhai, X. (2021). Structural styles and evolution of a thin-skinned fold-and-thrust belt with multiple detachments in the eastern Sichuan Basin, South China. *Journal of Structural Geology*, *142*, 104191. https://doi.org/10.1016/j.jsg.2020.104191

Gu, Z. D., Yin, J. F., Yuan, M., Bo, D. M., Liang, D. X., Zhang, H., & Zhang, L. (2015). Accumulation conditions and exploration directions of natural gas in deep subsalt Sinian-Cambrian System in the Eastern Sichuan Basin, SW China. *Petroleum Exploration and Development*, *42*(2), 152–166. https://doi.org/10.1016/S1876-3804(15)30002-1

Guenthner, W. R., Reiners, P. W., Ketcham, R. A., Nasdala, L., & Giester, G. (2013). Helium diffusion in natural zircon: Radiation damage, anisotropy, and the interpretation of zircon (U-Th)/He thermochronology. *American Journal of Science*, *313*(3), 145–198. https://doi.org/10.2475/03.2013.01

Guo, Z., Wang, K., Yang, Y. J., Tang, Y. C., John Chen, Y., & Hung, S. H. (2018). The origin and mantle dynamics of quaternary intraplate volcanism in northeast China from joint inversion of surface wave and body wave. *Journal of Geophysical Research: Solid Earth*, *123*(3), 2410–2425. https://doi.org/10.1002/2017JB014948

He, C. S. (2019). Evidence for an upwelling mantle plume beneath the Songliao basin, Northeast China. *Physics of the Earth and Planetary Interiors*, *297*, 106316. https://doi.org/10.1016/j.pepi.2019.106316

He, W. G., Zhou, J. X., & Yuan, K. (2018). Deformation evolution of Eastern Sichuan-Xuefeng fold-thrust belt in South China: Insights from analogue modelling. *Journal of Structural Geology*, *109*, 74–85. https://doi.org/10.1016/j.jsg.2018.01.002

Herrero-Barbero, P., Álvarez-Gómez, J. A., Martínez-Díaz, J. J., & Klimowitz, J. (2020). Neogene basin inversion and recent slip rate distribution of the northern termination of the Alhama de Murcia fault (Eastern Betic Shear Zone, SE Spain). *Tectonics*, *39*(7), e2019TC005750. https://doi.org/10.1029/2019TC005750

Horton, B. K. (2018). Tectonic regimes of the central and southern Andes: Responses to variations in plate coupling during subduction. *Tectonics*, *37*(2), 401–679. https://doi.org/10.1002/2017TC004624

Hu, J. P., Zhao, J. L., Wang, W. B., & Li, N. (2005). Relation of deep geophysics fields and rupture construct in Yangtse Gorges Chongqing reservoir area. *Journal of Earth Sciences and Environment*, *27*(03), 49–54.

Hu, W. S., Zeng, T., Zhou, Y. L., Yao, Q. K., & Tang, J. G. (2011). Applying balanced-restoring technique with detachment horizon profile to study the tectonic evolution. *Geoscience*, *25*(05), 896–901.

Hu, Z. Q., Zhu, G., Liu, G. S., & Zhang, B. L. (2009). The folding time of the Eastern Sichuan Jura-type fold belt: Evidence from unconformity. *Geological Review*, *55*(01), 32–42.

Hubbard, J., & Shaw, J. H. (2009). Uplift of the Longmen Shan and Tibetan plateau, and the 2008 Wenchuan (M = 7.9) earthquake. *Nature*, *458*(7235), 194–197. https://doi.org/10.1038/nature07837

Hughes, A. N., Benesh, N. P., & Shaw, J. H. (2014). Factors that control the development of fault-bend versus fault-propagation folds: Insights from mechanical models based on the discrete element method (DEM). *Journal of Structural Geology*, *68*, 121–141. https://doi.org/10.1016/j.jsg.2014.09.009

Hurford, A. J., & Green, P. F. (1983). The zeta age calibration of fission track dating. *Chemical Geology*, *41*, 285–317. https://doi.org/10.1016/s0009-2541(83)80026-6

Ji, W. B., Faure, M., Lin, W., Chen, Y., Chu, Y., & Xue, Z. H. (2018). Multiple emplacement and exhumation history of the late Mesozoic Dayunshan-Mufushan batholith in Southeast China and its tectonic significance: 1. Structural analysis and geochronological constraints. *Journal of Geophysical Research: Solid Earth*, *123*(1), 689–710. https://doi.org/10.1002/2017JB014597

Jia, X. L. (2016). *Structural geometry and kinematics of Southeast Sichuan Basin: Insights into tectonic relationship with the western segment of Xue Feng Mountain Orogenic Belt* (pp. 46–61). China University of Geoscience

Jiang, G. Z., Hu, S. B., Shi, Y. Z., Zhang, C., Wang, Z. T., & Hu, D. (2019). Terrestrial heat flow of continental China: Updated data set and tectonic implications. *Tectonophysics*, *753*, 36–48. https://doi.org/10.1016/j.tecto.2019.01.006

Ketcham, R. A., Carter, A., Donelick, R. A., Barbarand, J., & Hurford, A. J. (2007). Improved modeling of fission-track annealing in apatite. *American Mineralogist*, *92*(5–6), 799–810. https://doi.org/10.2138/am.2007.2281

Ketcham, R. A., Carter, A., & Hurford, A. J. (2015). Inter-laboratory comparison of fission track confined length and etch figure measurements in apatite. *American Mineralogist*, *100*(7), 1452–1468. https://doi.org/10.2138/am-2015-5167

Kohn, B., & Gleadow, A. J. W. (2018). *Application of low-temperature thermochronology to craton evolution on in fission-track thermochronology and its application to geology* (pp. 373–393). Springer International Publishing. https://doi.org/10.1007/978-3-319-89421-8_2

Konstantinovskaya, E. A., Rodriguez, D., Kirkwood, D., Harris, L. B., & Theriault, R. (2009). Effects of basement structure, sedimentation and erosion on thrust wedge Geometry: An example from the Quebec Appalachians and Analogue Models. *Bulletin of Canadian Petroleum Geology*, *57*(1), 34–62. https://doi.org/10.2113/gscpgbull.57.1.3

Koyi, H. A., & Cotton, J. (2004). Experimental insights on the geometry and kinematics of fold-and-thrust belts above weak, viscous evaporitic décollement: Discussion. *Journal of Structural Geology*, *26*, 2139–2141. https://doi.org/10.1016/j.jsg.2004.04.001

Koyi, H. A., & Mansurbeg, H. (2020). The role of multiple weak lithologies in the deformation of cover units in the northwestern segment of the Zagros fold-and-thrust belt. *Journal of Petroleum Geology*, *44*(2), 145–166. https://doi.org/10.1111/jpg.12783

Koyi, H. A., & Sans, M. (2006). Deformation transfer in viscous detachments: Comparison of sandbox models to the South Pyrenean Triangle Zone. *Geological Society, London, Special Publications*, *253*(1), 117–134. https://doi.org/10.1144/GSL.SP.2006.253.01.06

Koyi, H. A., & Vendeville, B. C. (2003). The effect of décollement dip on geometry and kinematics of model accretionary wedges. *Journal of Structural Geology*, *25*(9), 1445–1450. https://doi.org/10.1016/S0191-8141(02)00202-X

Kyle, K. (1996). Transition from basement-involved to thin-skinned thrusting in the Cordillera Oriental of southern Bolivia. *Tectonics*, *15*(4), 763–775. https://doi.org/10.1029/95

Lachenbruch, A., & Sass, H. (1977). Heat flow in the United States and the thermal regime of the crust. In *The Earth's Crust, its nature and physical properties. Geophysical Monograph* (Vol. 20, pp. 626–675). https://doi.org/10.1029/GM020p0626

Li, C. X., He, D. F., Lu, G., Wen, K., Simon, A., & Sun, Y. P. (2021). Multiple thrust detachments and their implications for hydrocarbon accumulation in the northeastern Sichuan Basin, southwestern China. *AAPG Bulletin*, *105*(2), 357–390. https://doi.org/10.1306/07272019064

Li, C. X., He, D. F., Sun, Y. P., He, J. Y., & Jiang, Z. X. (2015). Structural characteristic and origin of intra-continental fold belt in the eastern Sichuan basin, South China Block. *Journal of Asian Earth Sciences*, *111*, 206–221. https://doi.org/10.1016/j.jseaes.2015.07.027

Li, H. L., Zhang, Y. Q., Dong, S. W., Zhang, J. L., Sun, Y. J., & Wang, Q. M. (2020). Neotectonics of the Bailongjiang and Hanan faults: New insights into late Cenozoic deformation along the eastern margin of the Tibetan Plateau. *Geological Society of America Bulletin*, *132*(9–10), 1845–1862. https://doi.org/10.1130/B35374.1

Li, J. H., Cawood, P. A., Ratschbacher, L., Zhang, Y. Q., Dong, S. W., Xin, Y. J., et al. (2020). Building Southeast China in the late Mesozoic: Insights from alternating episodes of shortening and extension along the Lianhuashan fault zone. *Earth-Science Reviews*, *201*, 103056. https://doi.org/10.1016/j.earscirev.2019.103056

Li, J. H., Dong, S. W., Cawood, P. A., Zhao, G. C., Johnston, S. T., Zhang, Y. Q., & Xin, Y. J. (2018). An Andean-type retro-arc foreland system beneath northwest South China revealed by SINOPROBE profiling. *Earth and Planetary Science Letters*, *490*, 170–179. https://doi.org/10.1016/j.epsl.2018.03.008

Li, J. H., Shi, W., Zhang, Y. Q., Dong, S. W., & Ma, Z. (2016). Thermal evolution of the Hengshan extensional dome in central South China and its tectonic implications: New insights into low-angle detachment formation. *Gondwana Research*, *35*, 425–441. https://doi.org/10.1016/j.gr.2015.06.008

Li, J. H., Zhang, Y. Q., Dong, S. W., & Johnston, S. T. (2014). Cretaceous tectonic evolution of South China: A preliminary synthesis. *Earth-Science Reviews*, *134*, 98–136. https://doi.org/10.1016/j.earscirev.2014.03.008

Li, J. H., Zhang, Y. Q., Dong, S. W., & Li, H. L. (2012). Late Mesozoic-early Cenozoic deformation history of the Yuanma Basin, central South China. *Tectonophysics*, *570–571*, 163–183. https://doi.org/10.1016/j.tecto.2012.08.012

Li, S. J., Li, J. M., Zhou, Y., Wo, Y. J., & Wang, X. W. (2011). Fission track evidence for Mesozoic-Cenozoic uplifting in the southeastern margin of Sichuan basin. *Acta Petrologica et Mineralogica*, *30*(2), 225–233. https://doi.org/10.3969/j.issn.1000-6524.2011.02.007

Li, S. J., Xiao, K. H., Wang, X. W., Zhang, R. Q., Wo, Y. J., Zhou, Y., et al. (2008). Thermochronology of detrital minerals in the Silurian strata from Southern China and its geological implications. *Acta Geologica Sinica*, *8*, 1068–1076.

Li, S. Z., Suo, Y. H., Li, X. Y., Zhou, J., Santosh, M., Wang, P. C., et al. (2019). Mesozoic tectono-magmatic response in the East Asian ocean-continent connection zone to subduction of the Paleo-Pacific Plate. *Earth-Science Reviews*, *192*, 91–137. https://doi.org/10.1016/j.earscirev.2019.03.003

Li, X. M., & Shan, Y. H. (2011). Diverse exhumation of the Mesozoic tectonic belt within the Yangtze Plate, China, determined by apatite fission-track thermochronology. *Geosciences Journal*, *15*(4), 349–357. https://doi.org/10.1007/s12303-011-0037-5

Li, Z., Qiu, J. S., & Yang, X. M. (2014). A review of the geochronology and geochemistry of Late Yanshanian (Cretaceous) plutons along the Fujian coastal area of Southeastern China: Implications for magma evolution related to slab break-off and rollback in the Cretaceous. *Earth-Science Reviews*, *128*, 232–248. https://doi.org/10.1016/j.earscirev.2013.09.007

Li, Z. Q., Ran, L. H., Chen, G. S., Lu, Z. K., & Duan, X. G. (2002). Genetic geologic model and gas-bearing analysis of high and steep structures in east Sichuan. *Journal of Chengdu University of Technology*, *29*(6), 605–609.

Lin, W., Faure, M., Monie, P., Schaerer, U., Liangsheng, Z., & Yan, S. (2000). Tectonics of SE China; New insights from the Lushan massif (Jiangxi Province). *Tectonics*, *19*(5), 852–871. https://doi.org/10.1029/2000TC900009

Liu, J. H., Zhang, P., Lease, R. O., Zheng, D. W., Wan, J. L., Wang, W. T., & Zhang, H. P. (2013). Eocene onset and late Miocene acceleration of Cenozoic intracontinental extension in the North Qinling range-Weihe graben: Insights from apatite fission track thermochronology. *Tectonophysics*, *584*, 281–296. https://doi.org/10.1016/j.tecto.2012.01.025

Liu, S. F., Heller, P. L., & Zhang, G. W. (2003). Mesozoic basin development and tectonic evolution of the Dabieshan orogenic belt, central China. *Tectonics*, *22*(4), 1044. https://doi.org/10.1029/2002TC001390

Liu, S. F., Steel, R., & Zhang, G. W. (2005). Mesozoic sedimentary basin development and tectonic implication, northern Yangtze Block, eastern China: Record of continent-continent collision. *Journal of Asian Earth Sciences*, *25*(1), 9–27. https://doi.org/10.1016/j.jseaes.2004.01.010

Liu, S. G., Ma, W. X., Luba, J., Huang, W. M., Zeng, X. L., & Zhang, C. J. (2011). Characteristics of the shale gas reservoir in the lower Silurian formation, east Sichuan basin, China. *Acta Petrologica Sinica*, *27*(08), 2239–2252.

Liu, S. G., Yang, Y., Deng, B., Zhong, Y., Wen, L., Sun, W., et al. (2021). Tectonic evolution of the Sichuan Basin, Southwest China. *Earth-Science Reviews*, *213*, 103470. https://doi.org/10.1016/j.earscirev.2020.103470

Liu, S. Z. (1995). My opinion of structural pattern of thin-skinned structure in east Sichuan. *Acta Geologica Sichuan*, *15*(4), 264–267.

Liu, W., Qiu, N., Xu, Q., & Liu, Y. (2018). Precambrian temperature and pressure system of Gaoshiti-Moxi block in the central paleo-uplift of Sichuan Basin, Southwest China. *Precambrian Research*, *313*, 91–108. https://doi.org/10.1016/j.precamres.2018.05.028

Liu, X., Zhao, D. P., Li, S. Z., & Wei, W. (2017). Age of the subducting Pacific slab beneath East Asia and its geodynamic implications. *Earth and Planetary Science Letters*, *464*, 166–174. https://doi.org/10.1016/j.epsl.2017.02.024

Liu, Z. N., & Koyi, H. A. (2013). The impact of a weak horizon on kinematics and internal deformation of a failure mass using discrete element method. *Tectonophysics*, *586*, 95–111. https://doi.org/10.1016/j.tecto.2012.11.009

Lu, L. L., Jiang, S. H., Li, S. Z., Wang, P. C., Jiang, Y., Wang, G., et al. (2020). Evolution of Meso-Cenozoic subduction zones in the ocean-continent connection zone of the eastern South China Block: Insights from gravity and magnetic anomalies. *Gondwana Research*, *102*, 151–166. https://doi.org/10.1016/j.gr.2020.12.010

Massoli, D., Koyi, H. A., & Barchi, M. R. (2006). Structural evolution of a fold and thrust belt generated by multiple décollements: Analogue models and natural examples from the Northern Apennines (Italy). *Journal of Structural Geology*, *28*(2), 185–199. https://doi.org/10.1016/j.jsg.2005.11.002

Mei, L. F., Liu, Z. X., Tang, J. G., Shen, C. B., & Fan, Y. F. (2010). Mesozoic intra-continental progressive deformation in western Hunan-Hubei-eastern Sichuan provinces of China: Evidence from apatite fission track and balanced cross-section. *Earth Science Journal of China University of Geosciences*, *35*(02), 161–174.

Mitra, S. (2003). A unified kinematic model for the evolution of detachment folds. *Journal of Structural Geology*, *25*(10), 1659–1673. https://doi.org/10.1016/S0191-8141(02)00198-0

Mora, A., Casallas, W., Ketcham, R. A., Gomez, D., Parra, M., Namson, J., et al. (2015). Kinematic restoration of contractional basement structures using thermokinematic models: A key tool for petroleum system modeling. *AAPG Bulletin*, *99*(08), 1575–1598. https://doi.org/10.1306/04281411108

Morgan, J. K. (2005). Discrete element simulations of gravitational volcanic deformation: 1. Deformation structures and geometries. *Journal of Geophysical Research*, *110*(B5), B05402. https://doi.org/10.1029/2004JB003252

Mulugeta, G. (1988). Modelling the geometry of Coulomb thrust wedges. *Journal of Structural Geology*, *10*(8), 847–859. https://doi.org/10.1016/0191-8141(88)90099-5

Naylor, M., Sinclair, H. D., Willett, S., & Cowie, P. A. (2005). A discrete element model for orogenesis and accretionary wedge growth. *Journal of Geophysical Research*, *110*(B12), B12403. https://doi.org/10.1029/2003JB002940

Nilforoushan, F., Koyi, H. A., Swantesson, J. O. H., & Talbot, C. J. (2008). Effect of basal friction on surface and volumetric strain in models of convergent settings measured by laser scanner. *Journal of Structural Geology*, *30*(3), 366–379. https://doi.org/10.1016/j.jsg.2007.09.013

Northrup, C. J., Royden, L. H., & Burchfiel, B. C. (1995). Motion of the Pacific Plate relative to Eurasia and its potential relation to Cenozoic extension along the eastern margin of Eurasia. *Geology*, *23*(8), 719–722. https://doi.org/10.1130/0091-7613(1995)023<0719:MOTPPR>2.3.CO;2

Pollack, N. N., & Chapman, D. S. (1977). On the regional variation of heat flow, geotherms and lithosphere thickness. *Tectonophysics*, *38*(3–4), 279–296. https://doi.org/10.1016/0040-1951(77)90215-3

Qiu, N. S., Chang, J., Zhu, C. Q., Liu, W., Zuo, Y. H., Xu, W., & Li, D. (2022). Thermal regime of sedimentary basins in the Tarim, upper Yangtze and North China Cratons, China. *Earth-Science Reviews*, *224*, 103884. https://doi.org/10.1016/j.earscirev.2021.103884

Qiu, N. S., Feng, Q., Tenger, B., Shen, B. J., Ma, Z. L., Yu, L. J., et al. (2020). Yanshanian-Himalayan differential rectono-thermal evolution and shale gas preservation in Dingshan area, Southeastern Sichuan Basin. *Acta Petrolei Sinica*, *41*(12), 1610–1622. https://doi.org/10.7623/syxb202012013

Reiners, P. W. (2005). Zircon (U-Th)/He thermochronometry. *Reviews in Mineralogy and Geochemistry*, *58*(1), 151–179. https://doi.org/10.2138/rmg.2005.58.6

Reiners, P. W., & Brandon, M. T. (2006). Using thermochronology to understand orogenic erosion. *Annual Review of Earth and Planetary Sciences*, *34*(1), 419–466. https://doi.org/10.1146/annurev.earth.34.031405.125202

Ren, J. Y., Tamaki, K., Li, S. T., & Zhang, J. X. (2002). Late Mesozoic and Cenozoic rifting and its dynamic setting in eastern China and adjacent areas. *Tectonophysics*, *344*(3–4), 175–205. https://doi.org/10.1016/S0040-1951(01)00271-2

Replumaz, A., & Tapponnier, P. (2003). Reconstruction of the deformed collision zone between India and Asia by backward motion of lithospheric blocks. *Journal of Geophysical Research*, *108*(B6), 2285. https://doi.org/10.1029/2001JB000661

Richardson, N. J., Densmore, A. L., Seward, D., Fowler, A., Wipf, M., Ellis, M. A., et al. (2008). Extraordinary denudation in the Sichuan Basin: Insights from low-temperature thermochronology adjacent to the eastern margin of the Tibetan Plateau. *Journal of Geophysical Research*, *113*(B4), 1–23. https://doi.org/10.1029/2006JB004739

Roger, F., Jolivet, M., & Malavieille, J. (2010). The tectonic evolution of the Songpan-Garzê (North Tibet) and adjacent areas from Proterozoic to present: A synthesis. *Journal of Asian Earth Sciences*, *39*(4), 254–269. https://doi.org/10.1016/j.jseaes.2010.03.008

Rosas, F. M., Duarte, J. C., Almeida, P., Schellart, W. P., Riel, N., & Terrinha, P. (2017). Analogue modelling of thrust systems: Passive vs. Active hanging wall strain accommodation and sharp vs. Smooth fault-ramp geometries. *Journal of Structural Geology*, *99*, 45–69. https://doi.org/10.1016/j.jsg.2017.05.002

Shen, C. B., Mei, L. F., & Xu, S. H. (2009). Fission track dating of Mesozoic sandstones and its tectonic significance in the Eastern Sichuan Basin, China. *Radiation Measurements*, *44*(9–10), 945–949. https://doi.org/10.1016/j.radmeas.2009.10.001

Shen, X. M., Tian, Y. T., Zhang, G. H., Zhang, S. M., Carter, A., Kohn, B., et al. (2019). Late Miocene hinterland crustal shortening in the Longmenshan thrust belt, the eastern margin of the Tibetan plateau. *Journal of Geophysical Research: Solid Earth*, *124*(11), 11972–11991. https://doi.org/10.1029/2019JB018358

Shi, H. C., Shi, X. B., Glasmacher, U. A., Yang, X. Q., & Stockli, D. F. (2016). The evolution of eastern Sichuan basin, Yangtze block since Cretaceous: Constraints from low temperature thermochronology. *Journal of Asian Earth Sciences*, *116*, 208–221. https://doi.org/10.1016/j.jseaes.2015.11.008

Shi, H. C., Shi, X. B., Yang, X. Q., Jiang, H. Y., & Long, Y. K. (2011). Exhumation process of the Fangdoushan-Shizhu fold belt in Meso-Neozoic and its tectonic significance in western Hubei-eastern Chongqing. *Progress in Geophysics*, *26*(06), 1993–2002.

Shi, W., Dong, S. W., Zhang, Y. Q., & Huang, S. Q. (2015). The typical large-scale superposed folds in the central South China: Implications for Mesozoic intracontinental deformation of the South China Block. *Tectonophysics*, *664*, 50–66. https://doi.org/10.1016/j.tecto.2015.08.039

Shinn, Y. J., Chough, S. K., & Hwang, I. G. (2010). Structural development and tectonic evolution of Gunsan basin (Cretaceous-Tertiary) in the central Yellow Sea. *Marine and Petroleum Geology*, *27*(2), 500–514. https://doi.org/10.1016/j.marpetgeo.2009.11.001

Shu, L. S., Faure, M., Wang, B., Zhou, X. M., & Song, B. (2008). Late Paleozoic-early Mesozoic geological features of South China: Response to the Indosinian collision events in Southeast Asia. *Comptes Rendus Geoscience*, *340*(2–3), 151–165. https://doi.org/10.1016/j.crte.2007.10.010

Sternai, P., Jolivet, L., Menant, A., & Gerya, T. (2014). Driving the upper plate surface deformation by slab rollback and mantle flow. *Earth and Planetary Science Letters*, *405*, 110–118. https://doi.org/10.1016/j.epsl.2014.08.023

Sun, Y. J., Dong, S. W., Wang, X. Q., Liu, M., Zhang, H., & Shi, Y. L. (2022). Three-dimensional thermal structure of east Asian continental lithosphere. *Journal of Geophysical Research: Solid Earth*, *127*(5), e2021JB023432. https://doi.org/10.1029/2021JB023432

Suo, Y. H., Li, S. Z., Cao, X. Z., Wang, X. Y., Somerville, I., Wang, G. Z., et al. (2020). Mesozoic-cenozoic basin inversion and geodynamics in East China: A review. *Earth-Science Reviews*, *210*, 103357. https://doi.org/10.1016/j.earscirev.2020.103357

Tapponnier, P., Zhiqin, X., Roger, F., Meyer, B., Arnaud, N., Wittlinger, G., & Jingsui, Y. (2001). Oblique stepwise rise and growth of the Tibet plateau. *Science*, *294*(5547), 1671–1677. https://doi.org/10.1126/science.105978

Teixell, A., & Koyi, H. A. (2003). Experimental and field study of the effects of lithological contrasts on thrust-related deformation. *Tectonics*, *22*(5), 1054. https://doi.org/10.1029/2002TC001407

Tian, Y. T., Kohn, B. P., Gleadow, A. J. W., & Hu, S. B. (2013). Constructing the Longmen Shan eastern Tibetan Plateau margin: Insights from low-temperature thermochronology. *Tectonics*, *32*(3), 576–592. https://doi.org/10.1002/tect.20043

Tian, Y. T., Kohn, B. P., Phillips, D., Hu, S. B., Gleadow, A. J. W., & Carter, A. (2016). Late Cretaceous-earliest Paleogene deformation in the Longmen Shan fold-and-thrust belt, eastern Tibetan Plateau margin: Pre-Cenozoic thickened crust? *Tectonics*, *35*(10), 2293–2312. https://doi.org/10.1002/2016TC004182

Tian, Y. T., Kohn, B. P., Qiu, N. S., Yuan, Y. S., Hu, S. B., Gleadow, A. J. W., & Zhang, P. (2018). Eocene to Miocene out-of-sequence deformation in the eastern Tibetan plateau: Insights from shortening structures in the Sichuan Basin. *Journal of Geophysical Research: Solid Earth*, *123*(2), 1840–1855. https://doi.org/10.1002/2017JB015049

Tian, Y. T., Kohn, B. P., Zhu, C. Q., Xu, M., Hu, S. B., & Gleadow, A. J. W. (2012a). Post-orogenic evolution of the Mesozoic Micang Shan foreland basin system, central China. *Basin Research*, *24*(1), 70–90. https://doi.org/10.1111/j.1365-2117.2011.00516.x

Tian, Y. T., Qiu, N. S., Kohn, B. P., Zhu, C. Q., Hu, S. B., Gleadow, A. J. W., & McInnes, B. I. A. (2012b). Detrital zircon (U-Th)/He thermochronometry of the Mesozoic Daba Shan Foreland Basin, central China: Evidence for timing of post-orogenic denudation. *Tectonophysics*, *570–571*, 65–77. https://doi.org/10.1016/j.tecto.2012.08.010

Tian, Y. T., Zhu, C. Q., Xu, M., Rao, S., Barry, P. K., & Hu, S. B. (2011). Post-early Cretaceous denudation history of the northeastern Sichuan Basin: Constraints from low-temperature thermochronology profiles. *Chinese Journal of Geophysics*, *54*(3), 807–816.

Tong, Y. B., Jun, S. Y., Wu, Z. H., Mao, C. P., Pei, J. L., Yang, Z., et al. (2019). Passive crustal clockwise rotational deformation of the Sichuan Basin since the Miocene and its relationship with the tectonic evolution of the fault systems on the eastern edge of the Tibetan Plateau. *Geological Society of America Bulletin*, *131*(1–2), 175–190. https://doi.org/10.1130/B31965.1

Vermeesch, P. (2012). On the visualisation of detrital age distributions. *Chemical Geology*, *312–313*, 190–194. https://doi.org/10.1016/j.chemgeo.2012.04.021

Vermeesch, P. (2018). IsoplotR: A free and open toolbox for geochronology. *Geoscience Frontiers*, *9*(5), 1479–1493. https://doi.org/10.1016/j.gsf.2018.04.001

Wang, E., Kirby, E., Furlong, K. P., van Soest, M., Xu, G., Shi, X., et al. (2012). Two-phase growth of high topography in eastern Tibet during the Cenozoic. *Nature Geoscience*, *5*(9), 640–645. https://doi.org/10.1038/ngeo1538

Wang, E., Meng, K., Su, Z., Meng, Q. G., Chu, J. J., Chen, Z. L., et al. (2014). Block rotation: Tectonic response of the Sichuan basin to the southeastward growth of the Tibetan Plateau along the Xianshuihe-Xiaojiang fault. *Tectonics*, *33*(5), 686–718. https://doi.org/10.1002/2013TC003337

Wang, E., Meng, Q. R., Burchfiel, B. C., & Zhang, G. W. (2003). Mesozoic large-scale lateral extrusion, rotation, and uplift of the Tongbai-Dabie Shan belt in east China. *Geology*, *31*(4), 307–310. https://doi.org/10.1130/0091-7613(2003)031<0307:MLSLER>2.0.CO;2

Wang, P., Liu, S. F., Zheng, H. B., Wang, K., Gao, T. J., Pan, F., et al. (2012). Late-orogenic arcuate fold-thrust belts in northern Yangtze area: Structural characteristics and basin evolution. *Journal of Palaeogeography*, *15*(06), 819–838.

Wang, Y., Zhang, P. Z., Schoenbohm, L. M., Zheng, W. J., Zhang, B., Zhang, J. J., et al. (2018). Two-Phase exhumation along major shear zones in the SE Tibetan plateau in the late Cenozoic. *Tectonics*, *37*(8), 2675–2694. https://doi.org/10.1029/2018TC004979

Wang, Y. J., Fan, W. M., Zhang, G. W., & Zhang, Y. H. (2013). Phanerozoic tectonics of the South China block: Key observations and controversies. *Gondwana Research*, *23*(4), 1273–1305. https://doi.org/10.1016/j.gr.2012.02.019

Wenk, L., & Huhn, K. (2013). The influence of an embedded viscoelastic-plastic layer on kinematics and mass transport pattern within accretionary wedges. *Tectonophysics*, *608*, 653–666. https://doi.org/10.1016/j.tecto.2013.08.015

Willett, C. D., Fox, M., & Shuster, D. L. (2017). A helium-based model for the effects of radiation damage annealing on helium diffusion kinetics in apatite. *Earth and Planetary Science Letters*, *477*, 195–204. https://doi.org/10.1016/j.epsl.2017.07.047

Wolf, R. A., Farley, K. A., & Kass, D. M. (1998). Modeling of the temperature sensitivity of the apatite (U–Th)/He thermochronometer. *Chemical Geology*, *148*(1–2), 105–114. https://doi.org/10.1016/S0009–2541(98)00024-2

Wu, H., Qiu, N., Feng, Q., Chang, J., Jiang, K., Zhang, Y., et al. (2020). Reconstruction of tectonic uplift process with thermo-kinematic method. Chinese. *Journal of Geophysics*, *63*(06), 2329–2344. https://doi.org/10.6038/cjg2020N0438

Xie, G. A., Jia, D., Zhang, Q. L., Wu, X. J., Shen, L., Lv, Y. S., et al. (2013). Physical modeling of the Jura-type folds in eastern Sichuan. *Acta Geologica Sinica*, *87*(06), 773–788.

Xu, C. H., Zhang, L., Shi, H. S., Brix, M. R., Huhma, H., Chen, L. H., et al. (2017). Tracing an early Jurassic magmatic arc from South to east China Seas. *Tectonics*, *36*(3), 466–492. https://doi.org/10.1002/2016TC004446

Xu, W. L., Chen, J. H., Weng, A. H., Tang, J., Wang, F., Wang, C. G., et al. (2020). Stagnant slab front within the mantle transition zone controls the formation of Cenozoic intracontinental high-Mg andesites in northeast Asia. *Geology*, *49*(1), 19–24. https://doi.org/10.1130/g47917.1

Yamato, P., Kaus, B. J. P., Mouthereau, F., & Castelltort, S. (2011). Dynamic constraints on the crustal-scale rheology of the Zagros fold belt, Iran. *Geology*, *39*(9), 815–818. https://doi.org/10.1130/G32136.1

Yan, D. P., Xu, Y. B., Dong, Z. B., Qiu, L., Zhang, S., & Wells, M. (2016). Fault-related fold styles and progressions in fold-thrust belts: Insights from sandbox modeling. *Journal of Geophysical Research: Solid Earth*, *121*(3), 2087–2111. https://doi.org/10.1002/2015JB012397

Yan, D. P., Zhang, B., Zhou, M. F., Wei, G. Q., Song, H. L., & Liu, S. F. (2009). Constraints on the depth, geometry and kinematics of blind detachment faults provided by fault-propagation folds: An example from the Mesozoic fold belt of South China. *Journal of Structural Geology*, *31*(2), 150–162. https://doi.org/10.1016/j.jsg.2008.11.005

Yan, D. P., Zhou, M. F., Song, H. L., Wang, X. W., & Malpas, J. (2003). Origin and tectonic significance of a Mesozoic multi-layer over-thrust system within the Yangtze Block (South China). *Tectonophysics*, *361*(3–4), 239–254. https://doi.org/10.1016/S0040-1951(02)00646-7

Yang, Z., Shen, C. B., Ratschbacher, L., Enkelmann, E., Jonckheere, R., Wauschkuhn, B., & Dong, Y. P. (2017). Sichuan Basin and beyond: Eastward foreland growth of the Tibetan Plateau from an integration of Late Cretaceous-Cenozoic fission track and (U-Th)/He ages of the eastern Tibetan plateau, Qinling, and Daba Shan. *Journal of Geophysical Research: Solid Earth*, *122*(6), 4712–4740. https://doi.org/10.1002/2016JB013751

Yong, T., Fan, Y., Lv, Q. Q., Tang, W. J., & Wang, H. K. (2018). Analysis of the tectonic stress field of SE Sichuan and its impact on the preservation of shale gas in lower Silurian Longmaxi formation of the Dingshan region, China. *Journal of the Geological Society of India*, *92*(1), 92–100. https://doi.org/10.1007/s12594-018

Yuan, Y. S., Sun, D. S., Zhou, Y., Wang, X. W., Li, S. J., Zhang, R. Q., et al. (2010). Determination of onset of uplifting for the Mid-upper Yangtze area after Indosinian event. *Chinese Journal of Geophysics*, *53*(02), 362–369.

Zhang, B. L., Zhu, G., Hu, Z. Q., Xiang, B. W., Zhang, L., & Chen, Y. (2009). Numerical modeling and formation mechanism of the eastern Sichuan Jura-type folds. *Geological Review*, *55*(05), 701–711.

Zhang, X. Q., Shan, Y. H., Ni, Y. J., & Tan, Z. J. (2015). Numerical modeling of the Mesozoic east Sichuan fold belt: A two-stage tectonic model. *Geotectonica et Metallogenia*, *06*, 1022–1032.

Zhang, X. Q., Shan, Y. H., Nie, G. J., & Ni, Y. J. (2013). Numerical modeling of the Mesozoic east Sichuan fold belt: Influence of detachment depth on the fold pattern in the platform cover. *Geotectonica et Metallogenia*, *4*, 622–632.

Zhang, Y. Q., Dong, S. W., Li, J. H., & Qiu, E. K. (2021). Piecemeal delamination of thickened lithosphere triggered pulsed magmatism and mineralization during late Mesozoic intracontinental orogeny in East Asia. *Acta Geologica Sinica*, *95*(S1), 112–114. https://doi.org/10.1111/1755-6724.14849

Zhao, D. P. (2021). Seismic imaging of Northwest Pacific and East Asia: New insight into volcanism, seismogenesis and geodynamics. *Earth-Science Reviews*, *214*, 103507. https://doi.org/10.1016/j.earscirev.2021.103507

Zhao, D. P., Isozaki, Y., & Maruyama, S. (2017). Seismic imaging of the Asian orogens and subduction zones. *Journal of Asian Earth Sciences*, *145*, 349–367. https://doi.org/10.1016/j.jseaes.2017.06.016

Zhou, C., & Zhou, J. X. (2022). Relationship between Lateral/Basal shear stress ratio and structural vergence of thrust wedges: Results from analogue modeling and implications for the origin of eastern Sichuan–Xuefeng fold-thrust belt in South China. *Tectonics*, *41*(3), 1–22. https://doi.org/10.1029/2021TC007035

Zhu, C. Q., Qiu, N. S., Cao, H. Y., Liu, Y. F., & Jiang, Q. (2017). Tectono-thermal evolution of the eastern Sichuan Basin: Constraints from the vitrinite reflectance and apatite fission track data. *Earth Science Frontiers*, *24*(03), 94–104. https://doi.org/10.1002/gj.3779

Zhu, X. S., Zheng, H. W., Lu, M. J., & Zhang, Y. H. (2020). Lithospheric structure of the Xuefengshan belt, South China: Evidence from a seismic reflection profile. *Journal of Geodynamics*, *134*, 101688. https://doi.org/10.1016/j.jog.2019.101688

References From the Supporting Information

Farley, K. A., Wolf, R. A., & Silver, L. T. (1996). The effects of long alpha-stopping distances on (U-Th)/He ages. *Geochimica et Cosmochimica Acta*, *60*(21), 4223–4229. https://doi.org/10.1016/S0016-7037(96)00193-7

Hasebe, N., Barbarand, J., Jarvis, K., Carter, A., & Hurford, A. J. (2004). Apatite fission-track chronometry using laser ablation ICP-MS. *Chemical Geology*, *207*(3–4), 135–145. https://doi.org/10.1016/j.chemgeo.2004.01.007